Bull Volcanol (2014) 76:849
DOI 10.1007/s00445-014-0849-z

RESEARCH ARTICLE

The 3640–3510 BC rhyodacite eruption of Chachimbiro compound volcano, Ecuador: a violent directed blast produced by a satellite dome

Benjamin Bernard · Silvana Hidalgo · Claude Robin · Bernardo Beate · Jenny Quijozaca

Received: 28 January 2014 / Accepted: 7 July 2014 / Published online: 6 August 2014
© Springer-Verlag Berlin Heidelberg 2014

Abstract Based on geochronological, petrological, stratigraphical, and sedimentological data, this paper describes the deposits left by the most powerful Holocene eruption of Chachimbiro compound volcano, in the northern part of Ecuador. The eruption, dated between 3640 and 3510 years BC, extruded a ~650-m-wide and ~225-m-high rhyodacite dome, located 6.3 km east of the central vent, that exploded and produced a large pyroclastic density current (PDC) directed to the southeast followed by a sub-Plinian eruptive column drifted by the wind to the west. The PDC deposit comprises two main layers. The lower layer (L1) is massive, typically coarse-grained and fines-depleted, with abundant dense juvenile fragments from the outgassed dome crust. The upper layer (L2) consists of stratified coarse ash and lapilli laminae, with juvenile clasts showing a wide density range (0.7–2.6 g cm^{-3}). The thickness of the whole deposit ranges from few decimeters on the hills to several meters in the valleys. Deposits extending across six valleys perpendicular to the flow direction allowed us to determine a minimum velocity of 120 m s^{-1}. These characteristics show striking similarities with deposits of high-energy turbulent stratified currents and in particular directed blasts. The explosion destroyed most of the dome built during the eruption. Subsequently, the sub-Plinian phase left a decimeter-thick accidental-fragment-rich pumice layer in the Chachimbiro highlands. Juvenile clasts, rhyodacitic in composition (SiO_2=68.3 wt%), represent the most differentiated magma of Chachimbiro volcano. Magma processes occurred at two different depths (~14.4 and 8.0 km). The hot (~936 °C) deep reservoir fed the central vent while the shallow reservoir (~858 °C) had an independent evolution, probably controlled by El Angel regional fault system. Such destructive eruptions, related to peripheral domes, are of critical importance for hazard assessment in large silicic volcanic complexes such as those forming the Frontal Volcanic Arc of Ecuador and Colombia.

Keywords Chachimbiro · Ryodacite · Directed blast · Satellite dome · Physical volcanology · Thermobarometry

Editorial responsibility: S. De la Cruz-Reyna

Electronic supplementary material The online version of this article (doi:10.1007/s00445-014-0849-z) contains supplementary material, which is available to authorized users.

B. Bernard · J. Quijozaca
Universidad San Francisco de Quito, Diego de Robles y Vía Interoceánica, Quito, Ecuador

B. Bernard · S. Hidalgo
Instituto Geofísico, Escuela Politécnica Nacional, Ladrón de Guevara E11-253, Ap 17-2759 Quito, Ecuador

B. Bernard (✉) · C. Robin
Laboratoire Magmas et Volcans, Clermont Université, Université Blaise Pascal, CNRS-UMR 6524, IRD-R 163, Clermont-Ferrand, France
e-mail: bbernard@igepn.edu.ec

B. Beate
Departamento de Geología, Escuela Politécnica Nacional, Ladrón de Guevara E11-253, Ap 17-2759 Quito, Ecuador

Introduction

Pyroclastic density currents (PDCs) are mixtures of hot volcanic particles and gas that flow downslope under the influence of gravity. They are highly energetic and account for about a third of the total fatalities (278,800 deaths) due to volcanic activity worldwide since 1600 AD (Auker et al. 2013). Pyroclastic fallouts consist of volcanic particles that have traveled through the atmosphere before falling to the ground. They are not as threatening as PDCs but their widespread effects can produce severe economic loss (Oxford-Economics 2010) and even climatic changes (Pitari and Mancini 2002). In the last two decades, analogue modeling

and numerical simulations allowed major improvements concerning the knowledge of these phenomena. Nevertheless, the study of modern and ancient pyroclastic deposits remains fundamental to calibrate numerical models, elaborate future eruptive scenarios, and understand emplacement processes (Cas and Wright 1987).

Chachimbiro compound volcano (0°28' N, 78°17' W, 4034 m asl) is located 80 km north of Quito, in the northern part of the Ecuadorian Volcanic Front (EVF), the westernmost volcanic range related to the subduction of the Nazca Plate below South America (Fig. 1). In this region, Holocene activity is characterized by powerful but low-frequency explosive eruptions of acid andesite to dacite, with Volcanic Explosivity Index (VEI) ranging from 3 to 6, and by lava dome extrusions (Von Hillebrandt 1989; Andrade et al. 2014; Hall and Mothes 2008; Hidalgo et al. 2008; Robin et al. 2008). The long-lasting evolution of the Chachimbiro volcano comprises three successive phases named Huanguillaro, Tumbatú, and Hugá (Bernard et al. 2011). Only limited information is available on the Holocene activity of this volcano (Beate 2001), but recent investigation led the identification of at least four eruptions associated to the Hugá phase in the last 6,000 years (Bernard et al. 2011). In this paper, we date and study the deposits of the most important eruption from this period. This eruption left a complex well-preserved PDC deposit that crops out abundantly on the eastern side of the volcanic complex, in the Urcuquí district (Fig. 2). It also produced a pyroclastic fall deposit presently buried within the andisol of the Chachimbiro highlands.

The aim of this paper is to describe the 3640–3510 BC deposits in order to identify the source and the eruptive dynamics of this major eruption. Results of stratigraphical analysis as well as geochronological, geochemical, and physical volcanology studies are presented with a special focus on the most violent episode of the eruption: the emission of a high-energy PDC.

Methods

The PDC and fallout deposits have been sampled and studied in 95 locations in the field. Radiocarbon ages were obtained on six samples. Four age determinations were carried out by the LMC14 (Laboratoire de Mesure du Carbone 14), Bondy

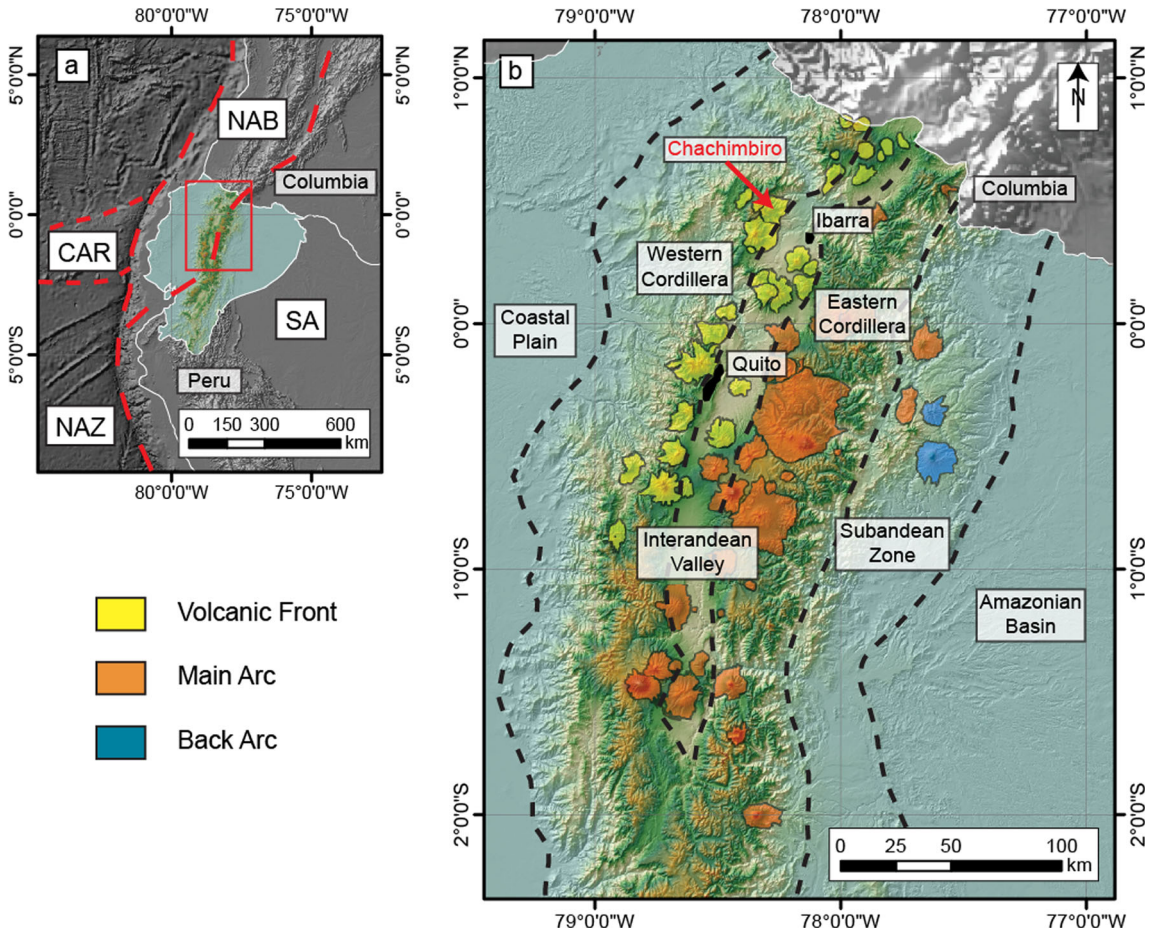

Fig. 1 **a** Geodynamic context of Ecuador, and **b** location of Chachimbiro volcano (modified from Monzier et al. 1997). *CAR* Carnegie Ridge; *NAB* North Andean Block; *NAZ* Nazca Plate; *SA* South American Plate

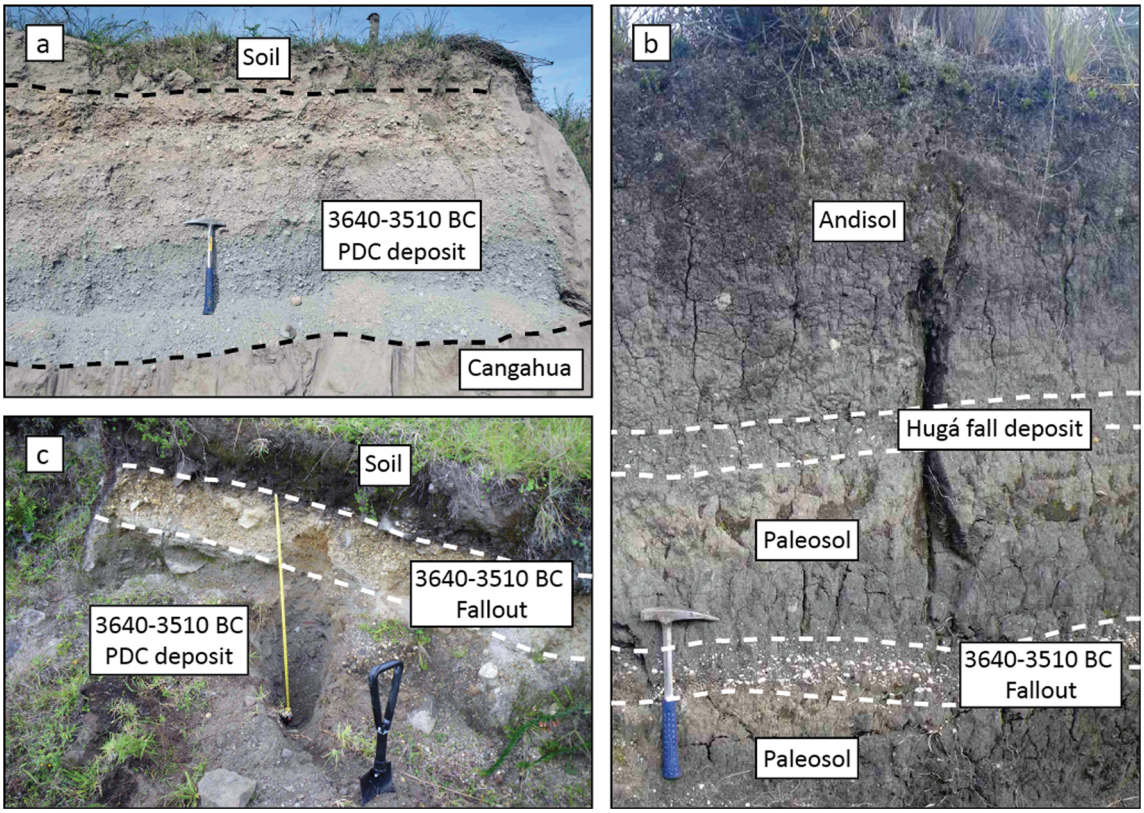

Fig. 2 Outcrops of the 3640–3510 years BC eruption deposits. **a** Quarry in the lowlands; **b** outcrop in Chachimbiro highlands showing the fallout layer and a younger fall deposit from Hugá edifice; **c** superposition of PDC and fall deposits

(France), using accelerator mass spectrometry (AMS). Two conventional determinations were obtained at the Center of Isotope Research, Groningen University (Netherlands), and using pre-treatment and analytical procedures described in Mook and Streurman (1983). Calibration of the ^{14}C ages was realized using OxCal 3.1 (Bronk Ramsey 2005) and atmospheric data from Reimer et al. (2004).

Major and trace element whole-rock analyses were carried out at the Université de Bretagne Occidentale. Chemical analyses were obtained on agate-ground powders by inductively coupled plasma–atomic emission spectroscopy (ICP-AES), except for Rb measured by flame atomic emission. Relative standard deviations are 1 % for SiO_2 and 2 % for the other major elements except for low concentrations (<0.50 %) for which absolute standard deviation is 0.01 %. Analytical procedure is described in detail in Cotten et al. (1995). Major element compositions for mineral and glasses were obtained at the Laboratoire Magmas et Volcans (Université Blaise Pascal, Clermont-Ferrand, France) using a CAMECA Camebax SX-100 electron microprobe, operating at 15 kV accelerating voltage, with a beam current of 15 nA for mineral analyses, and 8 nA and a 5-μm defocused beam for glass analyses. The estimated error for single analysis is of about 1 % when the element concentration is higher than 10 % and of 2–5 % when it is lower than 10 %.

Some physical characteristics of the deposit were observed and/or measured directly in the field (thickness, structure, and texture of the deposits). For the pyroclastic fallout deposit, the maximum clast size (both lithics and pumice) was obtained by measuring the three axes of the five largest clasts on an exposure surface of ~0.5 m^2 (Biass and Bonadonna 2011). The PDC deposits were mechanically sieved at 1−Φ intervals from −5 to 4Φ (i.e., from 32 mm to 64 μm, with $\Phi=-\log_2 d$, d being the particle diameter in millimeters) and weighed at 10^{-2} g for grain-size analysis. This study was completed with density measurements performed on the −4 to −5 Φ fraction (16–32 mm) using the method described in Houghton and Wilson (1989) and based on Archimedes' principle.

Age of the eruption

Three of the six radiocarbon ages were obtained on charcoal included in the PDC deposit. The other three come from two peat samples and a palaeosoil in the Chachimbiro highlands. The ages are consistent with the stratigraphy observed in the

Table 1 Radiocarbon age determinations and calendar age conversions. Calibration uses the OxCal 3.1 program (Bronk Ramsey 2005) and atmospheric data of the Intcal04 calibration curve (Reimer et al. 2004). Converted dates have a 1-year resolution but are rounded off to the nearest 5 years AD

Outcrop, sample and lab number[a]	Locality and UTM coordinates[b]	Sample material and deposit	$\delta^{13}C$ (‰)	Radiocarbon age (year BP ± 1σ)	Calendar age (year) 68.2% (1σ)[c]	Calendar age (year) 95.4% (2σ)[c]
CHA-BB-016	Munanyaro	Peat overlying the tephra deposit	−26.40	4,615 ± 40	**3500–3430 BC (46.4%)**	**3520–3330 BC (90.2%)**
D13	795231/48958				3380–3350 BC (21.8%)	3220–3180 BC (2.9%)
SacA 19708						3160–3130 BC (2.3%)
CHA-BB-009	San Francisco	Charcoal in the PDC deposit	−26.83	4,790 ± 65	**3650–3510 BC (68.2%)**	**3700–3490 BC (78.5%)**
D	810882/50134					
GrN-32372						3460–3370 BC (16.9%)
CHA-BB-021	Urcuquí	Charcoal in the PDC deposit	−23.58	4,765 ± 50	**3640–3510 BC (68.2%)**	**3650–3490 BC (77.0%)**
A	811661/47322					
GrN-32373						3460–3370 BC (18.4%)
CHA-BB-022	Pigunchuela	Charcoal in the PDC deposit	−25.00	4,760 ± 40	**3640–3520 BC (68.2%)**	**3640–3490 BC (81.3%)**
A	811359/47400					
SacA 19694						3430–3370 BC (14.1%)
CHA-BB-016	Munanyaro 795231/ 48958	Peat underlying the tephra deposit	−27.70	5,190 ± 40	4040–4010 BC (26.4%)	4230–4200 BC (1.3%)
D14						4160–4130 BC (2.4%)
SacA 19709					**4000–3960 BC (41.8%)**	**4070–3940 BC (90.6%)**
						3860–3820 BC (1.1%)
CHA-BB-014	Cochapata	Palaeosoil underlying the tephra deposit	−23.10	5,420 ± 40	**4335–4255 BC (68.2%)**	**4360–4220 BC (90.8%)**
A	804574/49391					
SacA 19693						4200–4160 BC (4.6%)

Values in bold correspond to the most probable calendar age

[a] Bondy and Groningen laboratory codes are given as SacA and GrN for AMS and PGC determinations, respectively

[b] UTM coordinates refer to the WGS 1984, Ecuador Zone 17 N

[c] Probability of the calendar age

field (Table 1). The palaeosoil (5,420±40 years BP) and the lower peat (5,190±40 years BP) give a maximum age for the eruption that is slightly younger than the age obtained on a palaeosoil (5,690±50 years BP) in the Chachimbiro highlands by Beate (2001). The upper peat gives a minimum age for the pyroclastic fall deposit (4,615±40 years BP). The consistency of the ages obtained on charcoal samples from the PDC deposit (Table 1) rules out any contamination process and allows calculation of a precise age for the event. Their combination leads to a single calibrated age of 3640–3510 years BC within a probability of 92.9 %.

In a sector called Cruz Tola, we found archaeological remains under the PDC deposit in the form of an irrigation channel. This indicates that there were human settlements in the Urcuquí district in the Early Formative Period (4400–1450 cal BC, Zeidler 2008). In this area there are also "Tolas", small mounds constructed by humans to celebrate religious rites. Archaeological investigations show that the "Tolas" were built by the Caranquis during the Late Period, between 1250 and 1550 AD (Moreira Pino 2012), and therefore not directly related to the irrigation channel. Abundant obsidian and ceramic fragments in this area indicate that the

Urcuquí district was an important place during pre-Columbian times.

Petrology of the juvenile samples

Whole-rock major and trace elements

SiO_2 contents of juvenile fragments from the PDC (five samples) and fallout (three samples) deposits range from 67.3 to 68.9 wt% (Table 2). Nevertheless, the PDC samples show a very narrow silica range (68.4±0.1 wt%). Since these blocks were collected in different localities, we consider their compositions representative of a homogeneous source. According to the classification of Peccerillo and Taylor (1976), the analyzed rocks are medium K-rich calc-alkaline rhyodacites (Fig. 3a). Compared to the whole Chachimbiro magmatic suite, which range from basaltic andesites to dacites, the 3640–3510 BC juvenile fragments are enriched in SiO_2 and depleted in MgO (Fig. 3b), as well as in FeO and CaO (not shown). Highly fractionated spectra for HREE are emphasized in the La/Yb vs. Yb diagram (Fig. 3c) where the high La/Yb ratios result from the Yb depletion in these rocks. In spider diagrams, they plot in the medium to upper part of the compositional range defined by the Chachimbiro rocks for the LILE (Cs, Rb, Ba, Th, Sr) and LREE (La and Ce). On the

Table 2 Whole-rock and trace element geochemical analysis for the 3640–3510 BC eruptive products. Major elements expressed as oxides in wt% and trace element concentrations in ppm

Sample Deposit	009-B PDC	018-A PDC	021-C PDC	019-A PDC	009-C PDC	016-P1-C9 Fallout	150-A Fallout	134-A Fallout
Major elements								
SiO_2	68.3	68.5	68.5	68.5	68.5	68.9	67.3	67.9
TiO_2	0.37	0.37	0.38	0.37	0.37	0.37	0.41	0.37
Al_2O_3	16.46	16.26	16.24	16.29	16.2	16.59	16.86	16.83
Fe_2O_3	3.18	3.16	3.23	3.15	3.21	2.53	4.11	3.32
MnO	0.045	0.045	0.046	0.044	0.045	0.041	0.045	0.047
MgO	1.12	1.14	1.14	1.1	1.12	1.17	1.2	1.1
CaO	3.67	3.75	3.75	3.75	3.76	3.85	3.85	3.76
Na_2O	4.78	4.78	4.71	4.75	4.75	4.63	4.56	4.59
K_2O	1.95	1.92	1.89	1.93	1.91	1.84	1.59	1.95
P_2O_5	0.11	0.11	0.11	0.11	0.12	0.12	0.08	0.12
Trace elements								
Sc	4.67	4.72	4.72	4.61	4.7	5.03	5.05	4.89
V	67.2	68.2	70.2	68.1	68.2	52.5	82.0	69.8
Cr	9.2	9.1	9.0	8.9	8.6	7.6	8.5	8.0
Co	6.5	6.3	6.5	6.2	6.4	5.8	7.1	6.5
Ni	4.3	4.6	4.5	4.0	3.9	4.6	4.9	5.9
Rb	33.0	43.7	36.2	42.3	44.4	31.1	31.2	43.0
Sr	521	526	527	527	519	535	557	535
Y	4.3	4.2	4.2	4.1	4.3	4.0	3.4	4.5
Zr	50.3	50.8	51.6	50.7	51.1	51.3	55.4	50.0
Nb	2.9	2.9	2.8	3.0	2.9	3.4	3.3	3.1
Ba	811	829	832	825	827	803	748	832
La	8.1	8.1	8.7	7.8	8.2	8.5	7.6	8.3
Ce	16.7	14.8	15.1	14.7	16.8	15.3	14.2	16.1
Nd	8.5	8.5	8.9	8.2	8.4	8.6	6.6	8.7
Sm	1.56	1.91	1.65	1.66	1.83	1.54	1.28	1.67
Eu	0.64	0.53	0.71	0.61	0.69	0.59	0.31	0.57
Gd	1.62	1.34	1.66	1.76	1.57	1.18	0.99	1.25
Dy	0.91	0.97	1.07	0.91	1.01	0.82	0.5	0.92
Er	0.03	0.08	0	0.02	0	0.51	0.36	0.17
Yb	0.31	0.31	0.31	0.28	0.31	0.27	0	0.34
Th	2.55	2.48	2.48	2.52	2.72	1.87	0.93	1.89
LOI	0.46	0.14	0.44	0.96	0.71	1.97	3.08	2.74

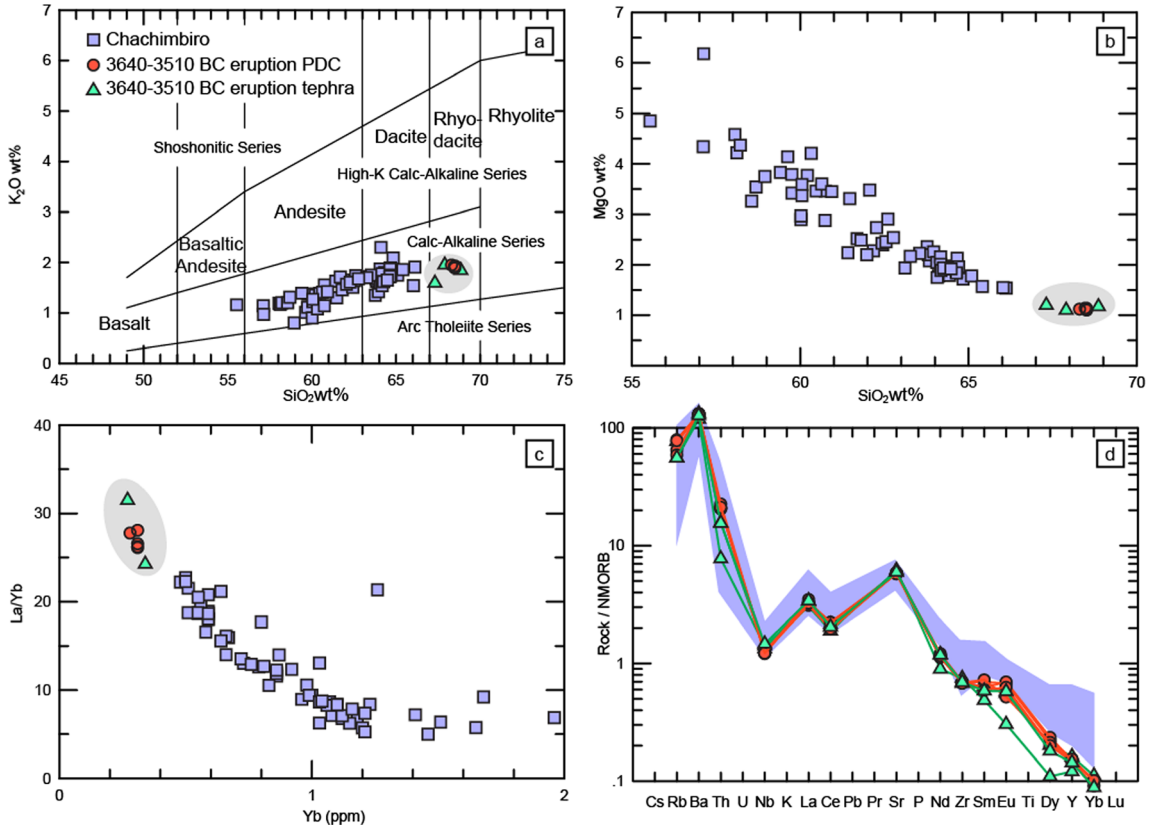

Fig. 3 **a** Classification diagram for volcanic arc rocks (Peccerillo and Taylor 1976). **b** MgO vs. SiO_2 (wt%) diagram showing strong differentiation of 3640–3510 BC samples with respect to other rocks of Chachimbiro compound volcano. **c** La/Yb vs. Yb diagram; high La/Yb ratios are mainly due to Yb depletion. **d** Spider diagrams normalized to N-MORB composition by Sun and McDonough (1989)

contrary, the analysis show a progressive depletion in MREE (Sm and Eu), HREE (Dy and Yb), and Y (Fig. 3d). Spider diagrams also show Nb negative anomaly typical of arc magmas. Globally, even though the 3640–3510 BC products appear more differentiated than the other samples from Chachimbiro compound volcano, they follow the same geochemical trend. Thus, we consider that they most likely come from the Chachimbiro magmatic system.

Petrography and mineral chemistry

The juvenile samples from the PDC deposit have a porphyritic-microlitic texture with about 30 vol% of phenocrysts. Textural banding due to variable degrees of vesicularity is also observed. The phenocryst mineral assemblage is composed of plagioclase (15 vol%)+amphibole (9 vol%)+Fe-Ti oxides (3 vol%)+biotite (2 vol%)+quartz (1 vol%)+traces of apatite (Fig. 4). The groundmass consists of 80 vol% of plagioclase, amphibole, Fe-Ti oxides and quartz microlites, and 20 vol% rhyolitic glass. Microprobe analyses are presented in the Online Resource 1.

Plagioclase is the most abundant phase (Fig. 5a), present as zoned phenocrysts, xenocrysts, inclusions in amphibole, and microlites. Euhedral phenocrysts (between 1 and 2.5 mm in size) show mostly reverse zoning with Na-rich cores (An 33.6 ±3.0 mol%) evolving to more Ca-rich rims (An 41.4± 1.7 mol%). Xenocrysts are anhedral andesine with An contents of 43.5±2.6 mol%. Inclusions in amphibole display similar andesine compositions (An 47.4±3.9 mol%). Microlites consist of acicular plagioclase showing a homogeneous composition at the limit oligoclase-andesine (An 29.5± 0.7 mol%) indicating equilibrium conditions with the surrounding analyzed volcanic glass. *Amphibole* is present as green and brown euhedral phenocrysts (<1 mm) and microlites. According to the classification of Leake et al. (1997) they are magnesio-hornblende and tschermakite (Fig. 5b). No reaction rims are optically observed and no notable difference in composition occurs between the narrow margins of crystals (<20 μm) and the inner adjacent zones. This indicates that, prior to the eruption, the crystals were mostly in equilibrium with the magma and that the ascent to the surface was fast enough to avoid any destabilization (Rutherford and Hill 1993). *Fe-Ti oxides* are present as titano-magnetite and ilmenite, both as euhedral microphenocrysts (about 0.3 mm in size) and microlites (<100 μm), as well as inclusions in amphibole. Both oxides are present as individual crystals without forming solid exsolution. *Biotite* is present as euhedral pleochroic phenocrysts of

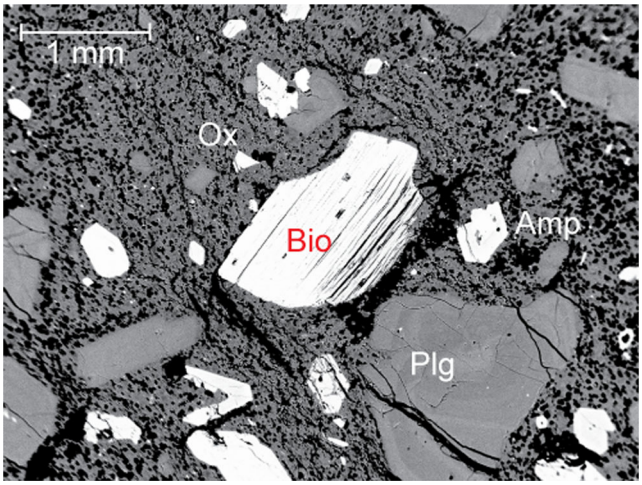

Fig. 4 Phenocryst assemblage in the 3640–3510 BC lava observed (microscope field, 5 mm). *Plg* plagioclase, *Amp* amphibole, *Ox* oxide; *Bio* biotite

about 1–3 mm long. Two slightly different compositions are observed (Mg#, 0.54–0.56; K_2O, 9.3 wt%; TiO_2, 3.6 wt%; and Mg#, 0.64–0.65; K_2O, 9.3 wt%; TiO_2, 2.8 wt%). *Quartz* is present as euhedral microphenocrysts and microlites. *Apatite* appears as an accessory phase (<1 vol%), present as euhedral microphenocrysts (<0.3 mm). The *volcanic glass* from the groundmass shows a very homogeneous rhyolitic composition (78.8±0.7 SiO_2 wt%).

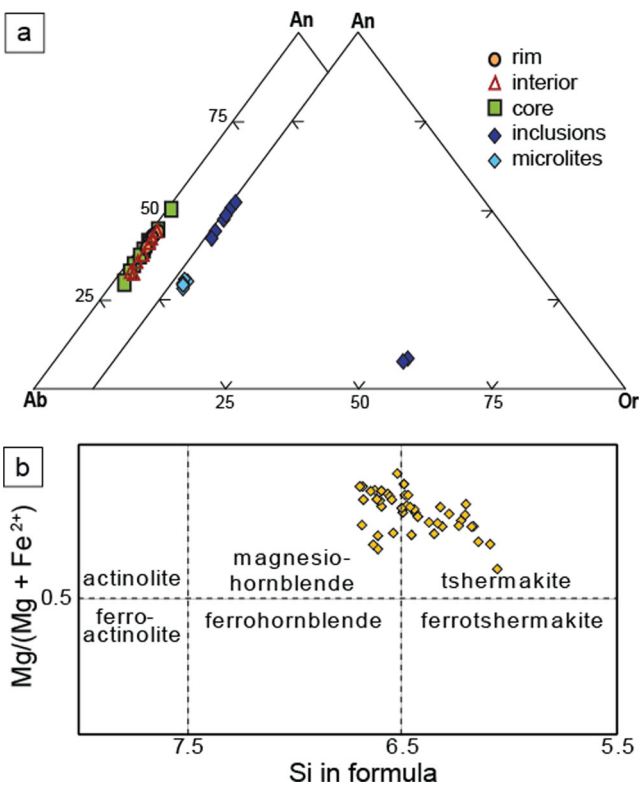

Fig. 5 Classification of minerals **a** Plagioclase classification of 3640–3510 BC eruption PDC juvenile products. Plagioclase phenocrysts vary from andesine to oligoclase. Two K-feldspars were also distinguished. *int* intermediate zones in phenocrysts; *inc* inclusions. **b** Amphibole compositions (cations in structural formula) plotted on the classification diagram of Leake et al. (1997)

Pre-eruptive conditions

Geo-barometry

Our mineralogical study has shown the crystallization of hornblende mostly at equilibrium with the surrounding melt. The Al-in-hornblende barometer is based on the increase of Al in hornblende as a function of pressure (Johnson and Rutherford 1989). We used the new empirical thermobarometric formulations from Ridolfi et al. (2010), which are based on a rigorous analysis of the physical-chemical, compositional and textural relationships of amphibole stability. These authors considered experimental results, H_2O-CO_2 solubility models, as well as natural amphibole-bearing calc-alkaline products. We applied their formulations to the amphibole and found two groups of amphibole cores associated to different crystallization pressures. The first group displays an equilibrium pressure of 408 ±30 Mpa (1 sigma SD) and the second of 228±33 Mpa (Table 3) the presence of two magmatic reservoirs. The corresponding depths are respectively 14.4±1 km and 8.0±1.1 km.

Geo-thermometry and oxygen fugacity

Ridolfi et al. (2010) formulations allow also the estimation of equilibrium temperature and oxygen fugacity (Table 3). The higher-pressure amphibole was formed at temperatures of 936 ±22 °C with a log fO_2 of −10.6±0.4 (ΔNNO 0.58±0.29). The temperatures calculated for the amphibole that crystallized at shallower depth are lower (858±22 °C) with a log fO_2 of −11.5±0.3 (ΔNNO 1.10±0.3). High water contents are estimated with these formulations, with H_2O of 7.8±0.4 wt% for the deeper amphibole and 7.1±0.5 wt% for shallower amphibole. These values are supported by the presence of euhedral biotite in the 3640–3510 BC samples.

Given the pcresence of titano-magnetite and ilmenite, we applied the thermometric formulations based in on the equilibrium of these two oxides. The 19 oxide pairs that fulfilled the equilibrium requirement of Bacon and Hirschmann (1988) were used to apply the thermometric formulations of Andersen and Lindsley (1988) and Ghiorso and Evans (2008). Considering that the oxides' equilibrium should represent the nearest surface conditions we used the QUILF program (Andersen et al. 1998), first varying T and oxygen fugacity, in order to obtain an oxygen fugacity value to fix in a second run. The obtained log fO_2 was −11.7, a very close value to that obtained for the shallower amphibole. According to the QUILF calibration and fixing the oxygen fugacity and the pressure to 230 MPa for shallow-depth conditions, the average equilibrium temperature for the 19 pairs was 768±44 °C. The same oxide pairs were used in the FeTiOxideGeotherm (version 1.1)

Table 3 Pre-eruptive pressure, temperature and water content of the rhyodacite feeding the 3640–3510 BC eruption

Geothermometer/geobarometer	Reference	P (MPa)	T (°C)	H_2O wt%
Al-in-amphibole	Ridolfi et al. (2010)	408±30	936±22	7.8±0.4
Al-in-amphibole	Ridolfi et al. (2010)	228±33	858±22	7.1±0.5
Fe-Ti-oxides (QUILF)	Andersen et al. (1998)	230[a]	768±44	
FeTiOxideGeotherm (Fe-Ti)	Ghiorso and Evans (2008)		679±12	
FeTiOxideGeotherm (Fe-Mg)	Ghiorso and Evans (2008)		775±52	
Plg-liquid thermometer	Putirka (2008)		722±36	7[b]

[a] Fixed pressure for the temperature calculation using the Fe-Ti oxides thermometer

[b] Fixed water content for the temperature calculation using the plagioclase-liquid thermometer

application of Ghiorso and Evans (2008). This application releases two temperatures, one based in the Fe-Ti exchange (679±12 °C) and one in the Fe-Mg exchange (775±52 °C) with a ΔNNO of 1.65±0.02.

Finally, we used Eq. 24a from Putirka (2008) for a plagioclase-liquid thermometer. This equation allows estimating equilibrium temperature between liquid and plagioclase within an error of ± 36 °C. From 49 liquid–plagioclase pairs, only 14 satisfied the equilibrium condition where stated by the author ($KD_{Ab\text{-}An}$ for temperatures below 1,050 °C is of 0.1± 0.05). We tested Eq. 24a with a fixed water content of 7 wt% and a pressure of 230 MPa, both estimated with the shallow-depth amphibole. Calculated temperature is 722 °C (Table 3), consistent with those calculated with oxides pairs.

Physical characteristics of the deposits

PDC deposit

Mapping The PDC deposit is easily recognized all over the Urcuquí district along the roads and in small quarries (Fig. 2a). It covers a fan-shaped area of about 62 km^2 including the main towns of Urcuquí district (Urcuquí, Tumbabiro, and San Blas) (Fig. 6). The thickness of the PDC deposit ranges from a maximum of 15 m at the foot of the peak La Viuda to few decimeters near Urcuquí. High thickness values (>2 m) are found in the five principal valleys of the area (Cachiyacu, Chuspihuaycu, la Banda, Añaburo, and Pigunchuela). Overall, the deposit thickness increases toward the center of the deposit area and the northwest.

Stratigraphy The PDC deposit overlies directly either an indurated volcanic ash deposit (Fig. 2a) known in Ecuador as Cangahua (Hall and Mothes 1997) or a brown ash layer. In few outcrops, the brown layer is transformed into a soil. The basal contact is generally flat with few erosive features and burned vegetation. The top of the PDC deposit is also relatively flat and forms terraces in the valleys. The deposit shows a complex stratification with lateral thickness and facies variations. Thirty-seven sections of this deposit are presented in Fig. 7.

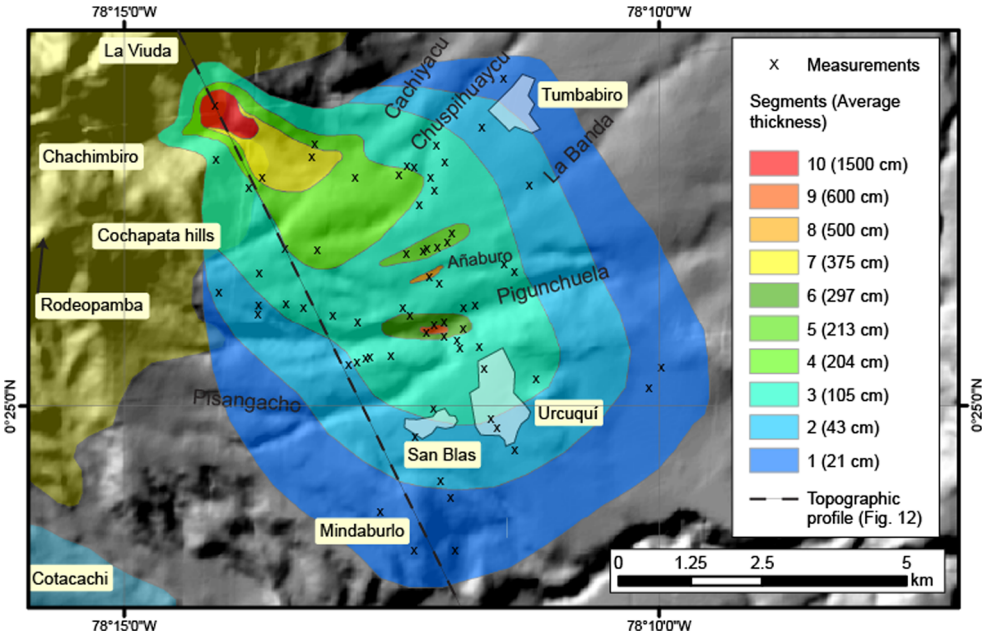

Fig. 6 Areal distribution and thickness of the 3640–3510 BC PDC deposit. The crosses correspond to thickness measurements carried out in 69 outcrops

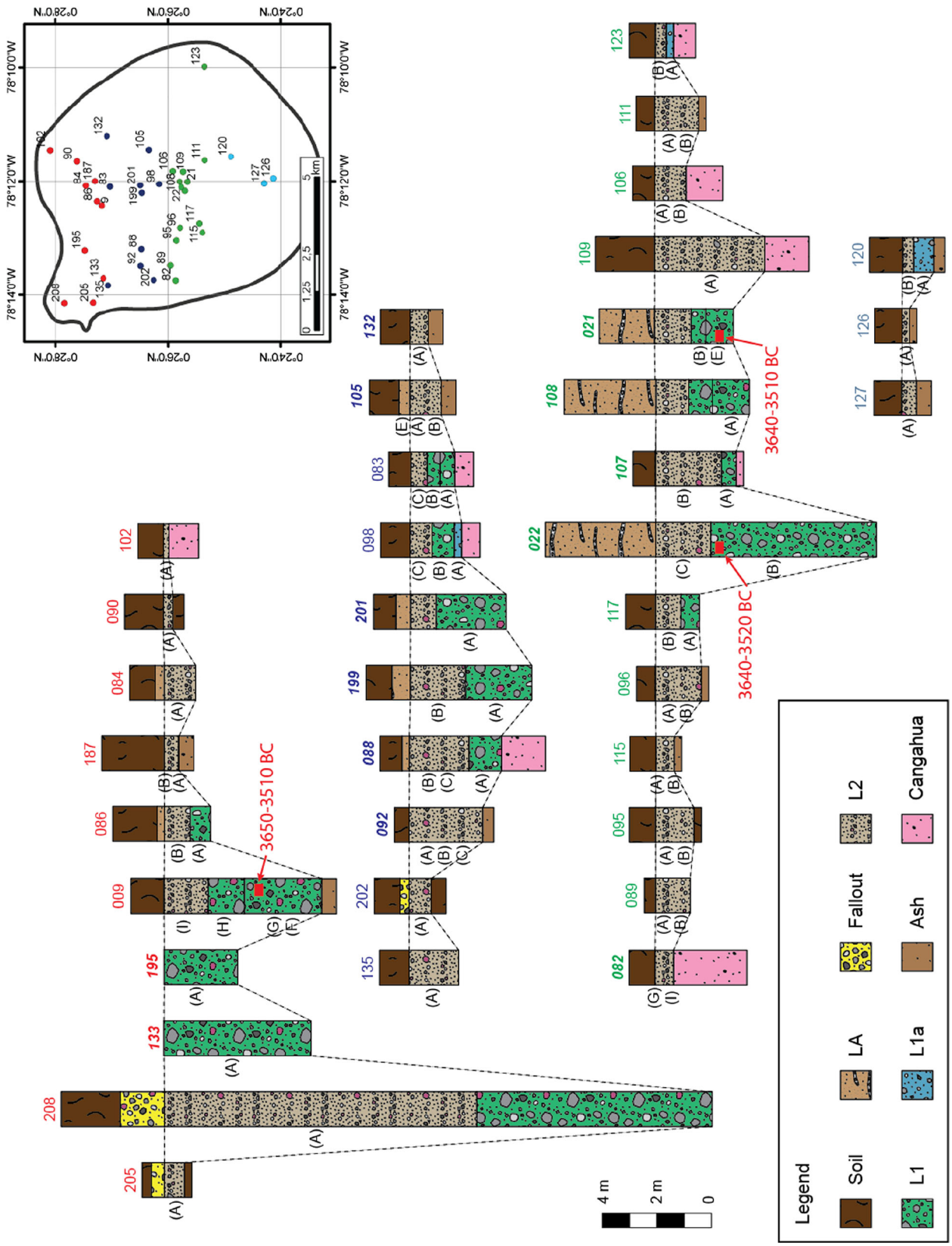

Fig. 7 Stratigraphic columns of the 3640–3510 BC PDC deposit with main units. Stratigraphic sections located in the valleys are in *bold italic* and *normal font* when located in the interfluves. The color of the stratigraphic columns corresponds to the sector where it was described (see the *inset map*). The *letters in brackets* correspond to the grain-size samples. Cal ^{14}C ages are in *red*

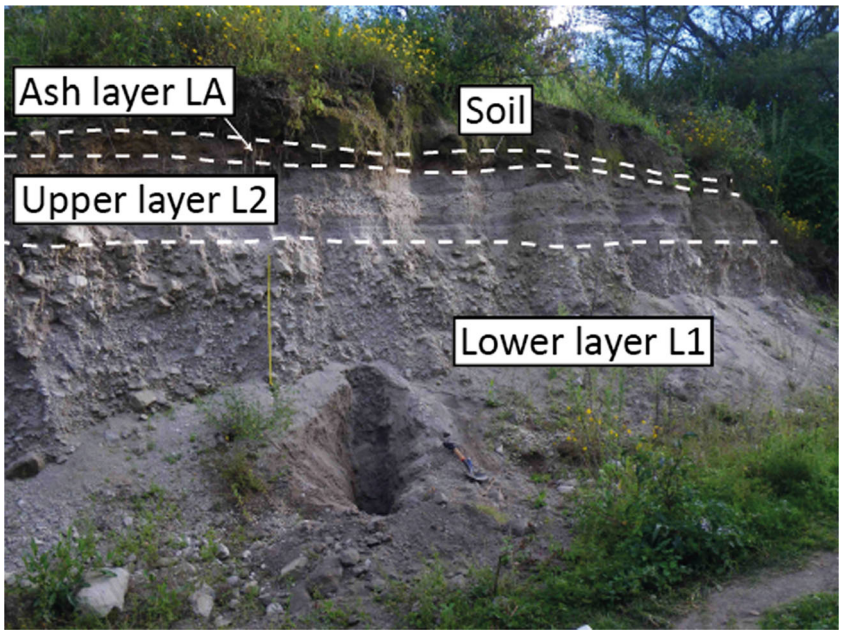

Fig. 8 Stratigraphy of the 3640–3510 BC PDC deposit

In order to present a comprehensive description, we simplified the deposit stratigraphy using the principal field characteristics. The deposit is principally composed of two layers (Fig. 8). The lower layer (L1) is a massive juvenile-rich pyroclastic deposit with some large rhyodacite blocks (>50 cm) and charcoal fragments. L1 is mostly concentrated in the valleys but can also be found in the interfluve areas. In some localities, this layer is roughly divided in two parts mostly due to difference of coloration (columns 009, 021, 083, and 108). The top of L1 displays gas escape structures. This layer contains banded and prismatic jointed blocks, and accidental clasts that are mostly oxidized andesite and lutite from the cretaceous basement (Natividad and Rio Cala units; Vallejo et al. 2006). The amount of accidental material is higher near the Cachiyacu river. In some outcrops, a fine-grained basal layer (L1a) is found below or instead of L1. This layer is slightly laminated and is typically found in the interfluve area.

The upper layer (L2) is the most widespread and is found both in valleys and in interfluve areas. This layer consists of stratified coarse ash and lapilli laminae. L2 has a higher content in accidental material than L1 with scarce large blocks (>20 cm) although it remains mostly composed of juvenile material (>90 vol%).

An ash layer (LA) with lenses of lapilli is found on top of the upper layer (Fig. 8). This layer, that can be up to 3 m thick, appears mostly in the valleys and is interpreted as reworking of the fine material from the PDC deposit.

Volume As an isopach map would not correctly represent the spatial distribution of a topographically controlled deposit, the volume of the deposit has been estimated using the Crandell (1989) method. The area has been divided into 10 segments, and an average thickness is attributed to each one (Fig. 6). It is important to note that in each segment the standard deviation on the thickness values can reach 20 to 62 % (Table 4) suggesting a possible large uncertainty on the volume calculation. This method gives a total volume of about 55×10^6 m^3.

Density and vesicularity of clasts The juvenile material is a porphyritic-microlitic rhyodacite with variable vesicularity. Dense rock equivalent density has been measured by water pycnometry on five rock powders (<2 μm). The results give a

Table 4 Areas, average thicknesses, and volumes of the 3640–3510 eruption PDC deposit. Segment numbers correspond to those in Fig. 6

Segment	1	2	3	4	5	6	7	8	9	10	Total
Area	21.5	15.3	17.6	4.4	0.43	0.56	1.33	0.06	0.06	0.53	61.77
Measurements	7	10	31	5	6	5	2	1	1	1	69
Average thickness (cm)	21	43	105	204	213	297	375	500	600	1500	
Standard deviation (cm)	13	12	53	53	42	118	35	–	–	–	
Standard deviation (%)	62 %	29 %	50 %	26 %	20 %	40 %	9 %	–	–	–	
Volume (10^6 m^3)	4.55	6.58	18.39	8.98	0.92	1.66	4.99	0.30	0.35	7.94	54.65

Table 5 Density of juvenile clasts in the 16–32 mm fraction. Average density, vesicularity, and accidental content are balanced volumetrically

Sample	Unit	Juvenile clast measurements	Maximum density	Minimum density	Standard deviation	Average density	Average vesicularity (%)	Accidental content (%)
009-F	L1	54	2,478	1,528	190	2,126	18.2	2.8
009-G	L1	47	2,536	1,054	303	2,134	17.9	0.0
009-H	L1	40	2,407	1,439	234	2,163	16.8	0.0
018-B	L1	32	2,560	1,087	403	2,105	19.0	8.7
018-C	L1	33	2,520	1,292	263	2,246	13.6	6.0
021-B	L1	32	2,517	1,013	488	2,039	21.6	0.0
021-E	L1	82	2,473	998	457	2,044	21.4	5.7
022-B	L1	58	2,592	988	427	2,040	21.5	11.5
086-A	L1	71	2,528	969	308	2,152	17.2	4.2
098-B	L1	38	2,483	1,655	151	2,327	10.5	0.0
099-A	L1	44	2,480	674	357	2,186	15.9	8.1
107-A	L1	79	2,487	926	535	1,867	28.2	2.5
108-A	L1	63	2,545	1,020	404	2,153	17.2	1.3
117-A	L1	31	2,496	1,403	291	2,281	12.3	0.0
195-A	L1	50	2,459	1,009	358	2,038	21.6	3.3
198-A	L1	20	2,455	1,341	279	2,236	14.0	5.7
199-A	L1	46	2,467	1,001	464	2,055	21.0	0.0
201-A	L1	103	2,533	1,022	379	2,121	18.4	1.8
082-G	L2	26	2,518	2,068	79	2,390	8.1	37.8
083-C	L2	45	2,448	1,022	415	2,075	20.2	28.3
088-B	L2	26	2,412	838	584	1,862	28.4	2.1
089-A	L2	19	2,383	101	471	1,892	27.2	9.9
092-B	L2	34	2,464	1,006	553	1,905	26.7	21.5
095-A	L2	68	2,501	1,032	363	2,242	13.8	0.0
095-B	L2	24	2,459	862	486	2,115	18.7	7.0
096-B	L2	44	2,426	1,023	421	2,108	18.9	16.4
098-C	L2	40	2,517	709	569	1,795	31.0	21.5
099-E	L2	50	2,480	820	545	2,045	21.4	6.7
106-A	L2	94	2,483	893	431	2,115	18.7	4.7
109-A	L2	33	2,556	1,216	321	2,263	13.0	0.0
117-B	L2	15	2,446	1,202	413	1,989	23.5	0.0
135-A	L2	50	2,478	778	653	1,861	28.4	41.8

dense rock density of 2.60±0.05 g cm^{-3}. Bulk density measurements using the immersion method were carried out on 1,491 juvenile clasts from the lower and upper PDC layers (Table 5). The results show a wide range of densities varying from 0.67 to 2.59 g cm^{-3}. The maximum density measured confirms the dense rock density obtained by water pycnometry. Therefore, the density measurements were converted to vesicularity. The global vesicularity histogram, showing the volumetric abundance of clasts by range of vesicularity, indicates that the distribution of vesicularity in the PDC deposit is roughly bimodal (Fig. 9a). A principal mode appears for both layers at 5–10 % of vesicularity and a secondary mode at 50–55 % characterizes better the upper layer. L1 has about 80.4 vol% of dense clasts (vesicularity < 25 %) contrary to L2 which presents a higher content in vesicular clasts (28.1 vol%). These results indicate a vertical variation of the clasts vesicularity in the PDC deposit. Nevertheless, the global shape of the density histograms (Fig. 9a) is the same suggesting that the material came from the same explosion and the vertical evolution may be due to transport and sedimentation processes. We present two density histograms made with samples from the same outcrop that support this general trend (Fig. 9b, c).

Grain size distribution In general, the deposits consist mostly of very fine ash to coarse lapilli particles but also contain a low fraction of extremely fine ash (<63 μm or greater than 4φ) and blocks (>64 mm or less than −6 φ) (White and Houghton 2006). A detailed grain-size analysis was realized on 70 samples for the −5 to > 4 φ fractions (32 mm to <63 μm)

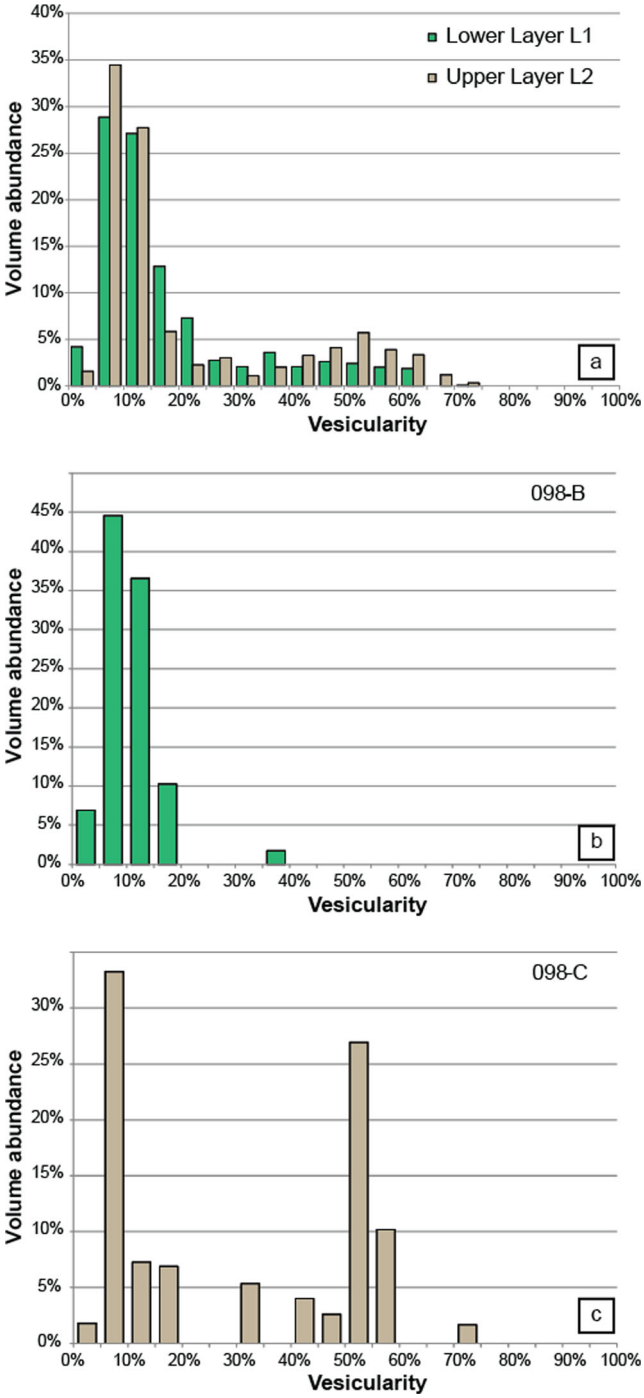

Fig. 9 **a** Vesicularity histograms of the main layers (L1 and L2) of the PDC deposit; the histogram for each unit has been created using the average of individual histograms (18 histograms for the lower layer L1 and 14 for the upper layer L2). **b** Vesicularity histogram of the sample 098-B from the lower layer L1 and **c** the sample 098-C from the upper layer L2. The abundance of clasts for each vesicularity range has been volumetrically balanced. Note the difference between the lower and upper layer in general and at outcrop scale, showing a vertical evolution

obtained by mechanical dry sieving. The extremely fine ash fraction represents about 2 % of the whole PDC deposit but variations from the base to the top from are notable: 1.3 wt% for the lower layer, 2.4 wt% for the upper layer. The layers L1a and LA present a higher amount of fines with 3.4 and 6.7 wt% respectively. The grain-size histograms (Fig. 10) and the Inman (1952) graphical statistics (Fig. 11, Online Resource 2) show that the PDC deposit displays broad grain-size distribution variability. The layer L1a is typically well sorted with a medium to very coarse ash mode and a normal distribution (Fig. 10a). L1 is relatively homogeneous and poorly sorted with a fine-medium lapilli mode and a positive skewness (Fig. 10b, c). L2 has the largest range of grain-size distribution from well sorted to poorly sorted with a grain-size mode ranging from medium ash to medium lapilli (Fig. 10d, e). The ash layer (LA) presents a medium ash mode at the limit between well sorted and poorly sorted (Fig. 10f). There is no evidence of longitudinal variation in L1. On the contrary, L2 changes from a fine-medium lapilli mode in the central area (Fig. 10d) to a coarse ash mode in the outer area (Fig. 10e). It is important to note that L2 usually displays laminae of coarse ash and fine-medium lapilli even in the outer area. As a whole, a crude normal grading characterizes the PDC deposit, except where L1a is present.

Taking into account this information, most of the PDC deposit shows the grain-size characteristics of pyroclastic surges and in particular directed blasts (Fig. 11). In general, the grain-size distribution in the PDC deposit is correlated to the facies. The coarser material is found in the valley facies and in Cachiyacu area while the finer material is represented in the outer zone and in the upper units in Pigunchuela area.

Pyroclastic fallout deposit

Distribution and stratigraphy The fallout deposit covers at least 70 km^2 with an elliptical shape elongated toward the west due to the dominant wind direction during the eruption. In the study area, the thickness of the fall deposit varies from 120 cm near Chachimbiro hot springs to 7 cm in the Western Cordillera highlands where it has been conserved in peat bogs. In the highlands, the fallout layer is found within the andisol at ~1.5 m depth, and about 0.5 m below a more recent lapilli fallout deposit from the Hugá phase (Fig. 2b). Near the peak La Viuda, the fallout lies directly on top of the upper unit of the PDC deposit (Fig. 2c). The eruption products are compositionally similar to those from the PDC deposit and consist of 80 vol% of rhyodacite pumices and 20 vol% of accidental material (principally lutite). These values correspond to an accidental-rich fallout. As the fallout is poorly exposed in the field, no grain-size or density analysis has been performed on this deposit.

Volume and plume height Thickness and maximum pumice size obtained in 25 outcrops allowed the interpretation of isopach and isopleth maps (Fig. 12; Online Resource 3). The

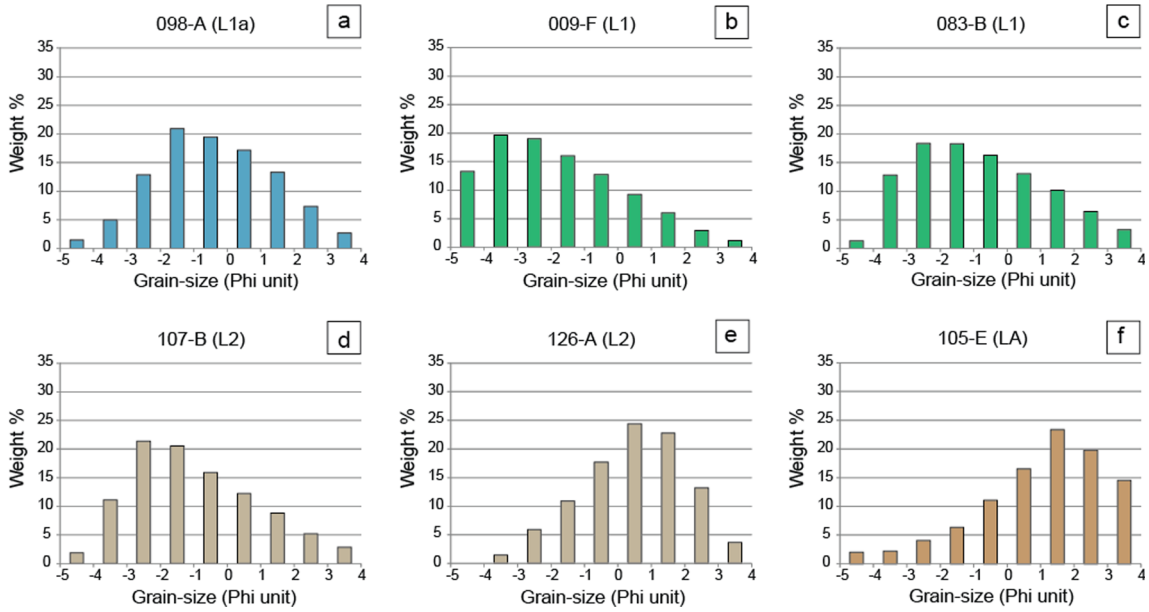

Fig. 10 Typical grain-size histograms of the main units of the PDC deposit. Grain-size ranges are in Phi units ($\Phi = -\log_2 d$)

volume of deposits (Table 6) has been estimated using different methods (Pyle 1989; Fierstein and Nathenson 1992; Legros 2000; Bonadonna and Houghton 2005; Bonadonna and Costa 2012). The result from the Power Law model has been discarded due to the low *m* coefficient (1.174). Bonadonna and Houghton (2005) show that a low *m* coefficient would produce a large uncertainty on the volume estimate. The exponential-1 segment (Pyle 1989) and 1 isopach (Legros 2000) models lead to low, unrealistic estimated volumes. The results from the exponential-2 segment (Fierstein and Nathenson 1992) and Weibull (Bonadonna and Costa 2012) models are similar and fit the data series better. Therefore, we use those to estimate a range of volumes (18–27 × 10^6 m^3). The plume height has been calculated at 13.5 km using the Weibull function (Bonadonna and Costa 2013).

Discussion

Eruption size and eruptive parameters

The parameters of the 3640–3510 BC eruption at Chachimbiro volcano are summarized in Table 7. According to the total volume of tephra (73–82 × 10^6 m^3) the eruption must be considered moderate to large with a Volcanic Explosivity Index of 3 (Newhall and Self 1982). This eruption is the largest Holocene eruption of Chachimbiro volcano. The Dense Rock Equivalent volume of the juvenile material is estimated at 49-53 × 10^6 m^3, which corresponds to 4.1 in magnitude (Pyle 2000). The intensity (9.8) and the height of the eruptive column (13.5 km) that produced the tephra fall ranks as sub-Plinian, similar to the 1992 Mount Spurr and 2006 Tungurahua eruptions (McGimsey et al. 2001; Eychenne et al. 2013). As

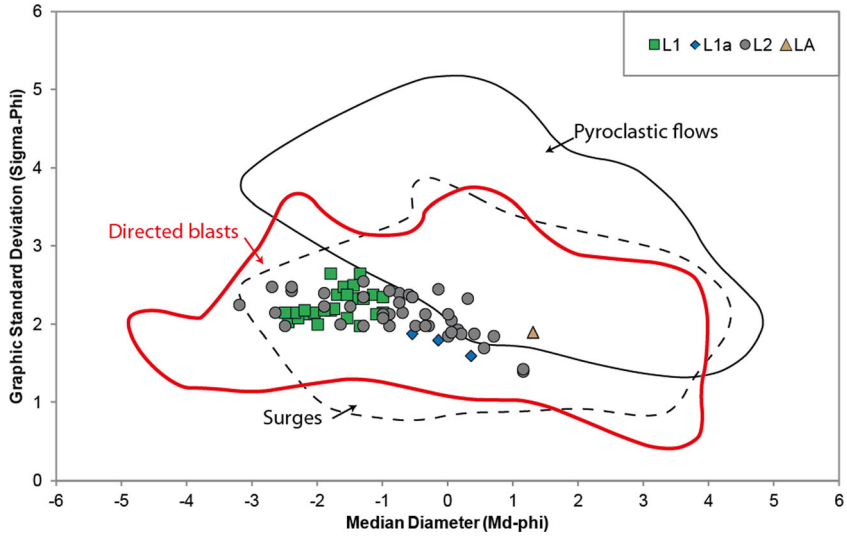

Fig. 11 Inman (1952) graphical parameters for the grain-size distribution of the PDC samples. The pyroclastic flows (*solid line*) and surge fields (dashed line) are from Walker (1971). The directed blast field (*red line*) is modified from Komorowski et al. (2013)

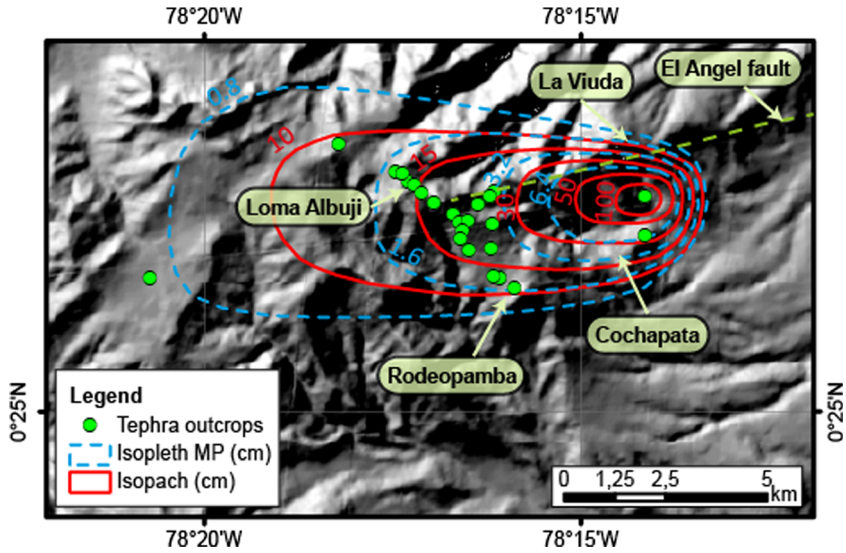

Fig. 12 Isopach and isopleth map of the fallout deposit. Main potential source locations of the eruption are indicated as well as the segment of El Angel fault

thickness variations in this topographically controlled deposit are important (Table 4), it is difficult to precisely determine the uncertainty for these results. As regards the PDC deposit, our field work (69 thickness measurements, >1 measurement/km^2) allows us to consider reliable our estimate of its volume. Conversely, due to the poor exposure of the pumice layer in the Chachimbiro highlands, our estimates for deposits of the sub-Plinian phase are tentative.

Source of the 3640–3510 BC eruption

Beate (2001) suggested that the source of the fallout deposit was a hill called Rodeopamba in eastern Chachimbiro foothills (Fig. 6 and 12). This hill, however, is covered by a thick andisol which includes the fallout deposit, as exposed in a recent road cut. Therefore, even if this hill represents the remains of a dome, the dome is older than the eruption. The PDC and fallout deposit maps (Fig. 6 and 12) indicate that the eruption did not come from the central vent (Loma Albují) or from the Cochapata hills. This interpretation is confirmed by the chemical composition of the PDC and fallout samples, which is clearly different from that of the rocks sampled in the highlands (Fig. 3). Isopach and isopleth maps clearly indicate a source from or close to the peak La Viuda (3314 m a.s.l.), about 6.3 km east of Chachimbiro summit, even though La Viuda peak is formed by old andesite lava flows from a former edifice belonging to the Huanguillaro construction phase (Bernard et al. 2011). At the base of the peak La Viuda, we observed an outcrop which consists of deformed shale belonging to the Cretaceous Natividad Unit (Vallejo et al. 2006). Clasts of this material are abundant in the eruption deposit, particularly in the fallout layer. Below La Viuda, on both sides of the Cachiyacu valley, large rhyodacite blocks with the same composition as in the eruption deposits are included in a landslide deposit. Therefore, we suggest that the source of the eruption was a moderate-sized dome emplaced in this valley at the foot of La Viuda peak at an altitude of 2,800–2,900 m asl. According to the calculated DRE volume (Table 7), this dome was probably about 600–700 m wide, and 200–250 m high. It is likely that most, if not all, of the dome was destroyed by the eruption. No further volcanic activity has been observed in this area. The source location coincides with a segment of the El Angel fault system that passes through Chachimbiro volcano (Fig. 12). This fault system marks the northern limit of the Ibarra Basin (Andrade 2009).

Table 6 Volume calculations for the 3640–3510 BC fallout deposit

Method	Author/parameters		R^2	Total volume (m^3)
1 isomass	Legros 2000/0.8 cm			1.34E+07
1 segment	Pyle 1989		0.946	1.18E+07
	Fierstein and Nathenson 1992		0.946	1.18E+07
2 segments	Fierstein and Nathenson 1992	Segment 1	0.960	1.80E+07
		Segment 2	1.000	
Power Law	Bonadonna and Houghton 2005/ m=1.174; C=[50;80]		0.994	5.07E+07–7.53E+07
Weibull	Bonadonna and Costa 2012		0.999	2.72E+07

Table 7 Eruptive size and parameters

	References	Equation/method	Value
Pyroclastic density current			
Opening angle of the deposit	Belousov et al. (2007)		100º
Area (A_{PDC})			62 km^2
Bulk volume (V_{PDC})	Crandell (1989)	Segments	55×10^6 m^3
Juvenile content (J_{PDC})			92 vol%
Estimated bulk density (δ_{PDC})	Glicken (1996)	Literature data	2.0 g cm^{-3}
Assumed magma density (δ_{magma})	Crosweller et al. (2012)	Literature data/dacite	2.4 g cm^{-3}
DRE volume (DRE_{PDC})		$V_{PDC}\times J_{PDC}\times\delta_{PDC}/\delta_{magma}$	42×10^6 m^3
Fallout			
Bulk volume (V_F)	Fierstein and Nathenson (1992), Bonadonna and Costa (2012)	Isopach map/exponential-2 segments, Weibull	18–27$\times10^6$ m^3
Column height (H)	Bonadonna and Costa (2013)	Isopleth map/Weibull	13.5 km
Wind velocity	Carey and Sparks (1986)	Isopleth map/0.8 cm	15 m s^{-1}
Juvenile content (J_F)			80 vol%
Estimated bulk density (δ_F)	Gardner and Tait (2000), Cobeñas et al. (2012)	Average of literature data for rhyodacite tephra	1.2 g cm^{-3}
Assumed magma density (δ_{magma})	Crosweller et al. (2012)	Literature data/dacite	2.4 g cm^{-3}
DRE volume (DRE_F)		$V_F\times J_F\times\delta_F/\delta_{magma}$	7–11$\times10^6$ m^3
Volumetric discharge rate (Q)	Mastin et al. (2009)	$Q=(H/2.00)^{1/0.241}$	2,760 m^3 s^{-1}
Mass eruption rate (MER)		$MER=Q\times\delta_{magma}$	6.6$\times10^6$ kg s^{-1}
Duration (D)		$D=DRE_F/Q$	43–65 min
Intensity (I)	Pyle (2000)	$I=\log_{10}[MER]+3$	9.8
Global eruption			
Tephra volume (V_T)		$V_T=V_{PDC}+V_F$	73–82$\times10^6$ m^3
Volcanic explosivity index (VEI)	Newhall and Self (1982)		3
DRE total (DRE)		$DRE=DRE_{PDC}+DRE_T$	49–53$\times10^6$ m^3
Magnitude (M)	Pyle (2000)	$M=\log_{10}[DRE\times\delta_{magma}]-7$	4.1

Eruptive dynamics

PDCs are hot mixtures of gas and volcanic particles driven by gravity (Druitt 1998; Branney and Kokelaar 2002). Such mostly turbulent currents are produced by various mechanisms including, but not limited to: (1) fallback or continuous fountaining of an eruptive mixture from a vertical eruption column; (2) gravitational collapse of a growing lava dome or a steep lava front; (3) rapid decompression of a shallow magmatic body (Valentine and Fisher 2000). PDC deposits are characterized by a large variety of facies with two end-members, pyroclastic flows and surges (Fisher and Schmincke 1984; Cas and Wright 1987; Branney and Kokelaar 2002). Pyroclastic surges are dilute currents forming deposits that mantle topography and tend to be thicker in depressions (Valentine 1987). Their deposits are typically laminated and enriched in dense lithics and crystals. There are several subtypes of pyroclastic surges: base surges, ash-cloud surges, ground surges, and lateral blasts (Druitt 1998). Pyroclastic flows are highly concentrated currents forming deposits controlled by topography and tending to pond in valleys. They are generally massive, and poorly sorted deposits. Sometimes, the deposits present a subtle grading of large clasts. This grading is inverse for vesicular pyroclasts and normal for dense pyroclasts. There are also subtypes of pyroclastic flows mostly based on the components of the deposit or depositional processes: i.e., ignimbrites, ash flows, scoria flows, block-and-ash flows (Cas and Wright 1987; Fisher 1990; Freundt et al. 2000). The distinction between a pyroclastic flow and a pyroclastic surge is not always obvious and it is probable that

a continuum of facies and processes exists between these two end-members (Wilson and Houghton 2000; Burgisser and Bergantz 2002).

In order to identify the source mechanism of this PDC, we have chosen two complementary approaches: (1) sedimentology of the PDC deposit; (2) mobility of the PDC.

The PDC deposit has the following characteristics:

- A fan-shaped deposit with an aperture angle of 100°. The deposit mantles the landscape with an irregular thickness showing pounding in the valleys;
- A crude stratification with at least one massive layer at the base and a more laminated layer to the top;
- A juvenile-rich deposit with a wide range of density and an apparent vertical evolution from poorly vesicular clasts at the base to highly vesicular clasts to the top;
- A generally fines-depleted, lapilli rich, well- to poorly sorted deposit.

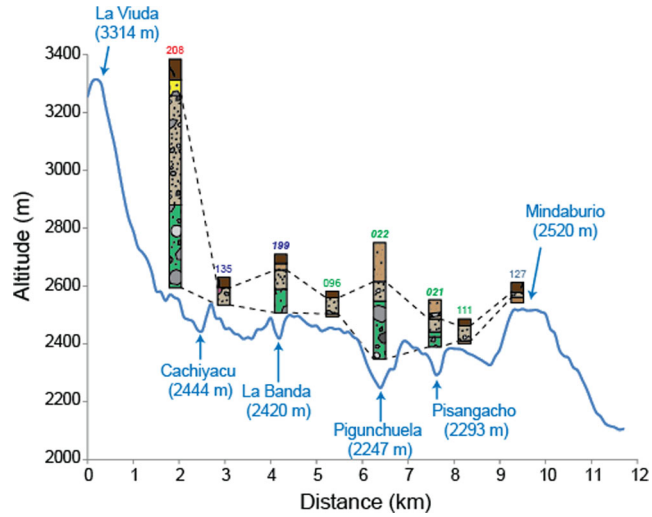

Fig. 13 Topographic profile between La Viuda peak and Mindaburio hill (see location in Fig. 6) with principal stratigraphic sections of the PDC deposit. The legend for the sections is the same as Fig. 7

Based on these characteristics, the 3640–3510 BC PDC deposit fits mostly the description of a high-energy turbulent stratified PDC deposit. In detail, these characteristics are very similar to those of directed blast deposits from decompression of highly pressurized cryptodomes such as at the eruption of Mount St. Helens in 1980 (Hoblitt et al. 1981) or lava domes (Pelean activity) such as at the eruption of Merapi volcano in 2010 (Komorowski et al. 2013). The graphical parameters of the grain-size distribution (Fig. 11) show also a great correspondence with surge and directed blast deposits. Also, the global vesicularity distribution (Fig. 9) is similar to that of the Bezymianny deposit (Belousov et al. 2007). Compared to other eruptions with directed blasts, the 3640–3510 BC event most resembles the Soufrière Hills and Merapi examples as we did not find the abundant soil erosion features described for Bezymianny and Mount St. Helens deposits (layer A in Belousov et al. 2007). Compared to the typical stratigraphy for blast deposits proposed by Belousov et al. (2007), the lower layer (L1) is similar to the layer B, while the upper layer (L2) has characteristics similar to those of the layer C. Komorowski et al. (2013) also describe bipartite units in the Merapi 2010 PDC deposit. They interpret the lower layer as the deposit of the erosive flow head while the upper layer corresponds to the turbulent upper part and wake of the PDC. This interpretation seems valid, and in particular explains the longitudinal and lateral variations of thickness and facies in the 3640–3510 BC PDC deposit. Below L1, the fine-grained basal layer (L1a) is interpreted as segregation of fines decoupling from the front of the PDC when it reaches a topographic barrier such as a transversal valley. This hypothesis agrees with the fact that this layer mostly occurs in the interfluve areas and also fits the experimental results obtained by Andrews and Manga (2011).

Some mobility factors have been calculated from the distribution of the PDC deposit. The travel distance (L) of the 3640–3510 BC eruption is about 10.5 km and the drop height (H) is estimated to be 800–900 m. The apparent friction coefficient (Heim 1932) of the 3640–3510 BC PDC (H/L= 0.076–0.086) is extremely low as well as the aspect ratio of the deposit (AR=3–4×10^{-4}; definition of Dade 2003). These parameters are clearly incompatible with typical dome collapses that have typical H/L>0.2 and AR>10^{-2} (Calder et al. 1999; Dade 2003; Saucedo et al. 2005). The low AR is common for surges and ignimbrites (Dade 2003), but the extremely low H/L (<0.1) is scarce. The mobility factor $A/V^{2/3}$ (Hayashi and Self 1992) calculated for the 3640–3510 BC PDC is around 515. This value is greater than those of dome-collapse flows (34±4) and relatively close to surges (430–460) of Soufrière Hills (Calder et al. 1999). This value is low compared to that of large directed blast associated to cryptodomes decompression (Bezymianny ~1,460; Mount St. Helens ~2,610) and intermediary compared to medium size directed blast associated to dome decompression (Soufrière Hills ~360; Merapi ~750; Montagne Pelée ~815) (Belousov et al. 2007; Komorowski et al. 2013). At Chachimbiro, the fact that the main dispersion axis of the PDC was oriented almost perpendicular to the local slope may explain the relatively low value of $A/V^{2/3}$ compared to Merapi and Montagne Pelée events.

The mobility of the PDCs can also be assessed using their ability to surmount obstacles. The 3640–3510 BC PDC crossed several valleys and was able to climb a hill at 8 km from the source. Using the height gained (H_G= 253 m) between the bottom of the Pigunchuela valley and the top of the Mindaburlo hill (Fig. 13), the calculated minimum velocity of the blast is about 70 m s^{-1} at 5 km from the source. A more realistic approach developed by Francis and Baker (1977) estimates a frictional loss (F)

that takes into account the height lost along the emplacement path (H_L=553–653 m):

$$F = 1-(H_G/H_L)^{1/2} \quad (1)$$

$$v = 10(2 \times g \times H_G/100 \times F)^{1/2} \quad (2)$$

This model gives 120–135 m s^{-1} at 5 km from the source. These results are compatible with velocities measured or inferred from other directed blasts (Belousov et al. 2007; Komorowski et al. 2013). According to Andrews and Manga (2011), PDCs do not pass barriers >1.5 times the current thickness. Therefore, the 3640–3510 BC PDC was at least 170 m thick at 8 km from the source.

Reconstruction of the 3640–3510 BC eruption

Magma storage, evolution and migration

The chemical composition of the 3640–3510 BC eruption products suggests that the magma was issued from the Chachimbiro magmatic system but that it underwent a more extended differentiation process than the other rocks from the compound volcano. Amphibole crystallization shows that this process occurred at two depths (about 14.4 and 8.0 km) correlated with a trend of decreasing temperatures. We propose that the hot deep reservoir is the main Chachimbiro magma reservoir while the shallow reservoir had an independent evolution from the Chachimbiro feeding system and is probably controlled by El Angel fault system. Because of differentiation processes or tectonic movements, the magma started its migration from the shallow reservoir toward the surface. As there is no evidence of disequilibrium on the minerals (in particular the amphiboles), this migration must have been relatively rapid. When the cool viscous magma reached the surface it accumulated as a lava dome, the external part of which cooled and outgassed.

Source-transport-depositional system of the PDC

We use the concept of a source-transport-depositional system developed by Fisher (1990) and modified by Komorowski et al. (2013) to describe the emplacement of the 3640–3510 BC PDC. The reason why the lava dome exploded is not known. Komorowski et al. (2013) observed that directed blasts are generally associated to domes or cryptodomes with very high growth rates. They suggest that elevated magma flux reduced the time required to outgas the inner part of the dome and create an overpressure inside the dome. This hypothesis is supported by the density measurements that indicate more highly vesicular juvenile fragments in L2 than in L1. In the case of the 3640–3510 BC eruption, it is probable that a part of the volatile-rich magma that participate to the sub-Plinian phase was stored in the conduit rather than in the lava dome. This magmatic column may have also exerted pressure on the lava dome. Based on the historical data available on Merapi, Soufrière Hills, and the Montagne Pelée, we propose a pre-blast dome growth rate of the order of 10 to 38 m^3 s^{-1} (Komorowski et al. 2013). According to the volume of magma erupted during the PDC phase, the dome growth phase must have lasted between 13 and 49 days.

Lateral or directed blasts related to the decompression of a gas-pressurized magma body may follow three scenarios: (1) explosion of a cryptodome as the result of a giant landslide (i.e., Bezymianny 1956, Mount St. Helens 1980; Hoblitt et al. 1981; Belousov 1996); (2) failure and explosion of a growing lava dome in association with a giant landslide (i.e., Tacana Late-pleistocene and Soufrière Hills 1997; Voight et al. 2002; Macías et al. 2010); (3) failure and explosion of a growing lava dome without giant landslide (i.e., Montage Pelée 1902 and Merapi 2010; Boudon et al. 2005; Komorowski et al. 2013). There is no evidence of a landslide scar or a debris avalanche deposit associated to the 3640–3510 BC eruption, so a simple dome failure and explosion seems likely. In the case of Merapi event, the directed blasts (at least two main episodes) are included in a complex series of volcanic processes such as retrogressive dome collapses (Charbonnier et al. 2013). The 3640–3510 BC PDC was different in that it was shortly followed by the sub-Plinian phase without previous or further activity. Therefore, we interpret the deposits of the PDC and fallout as the result of a monogenetic vent within the Chachimbiro volcano. The dome's failure could have been triggered by a combination of factors. The high growth rate probably produced a highly unstable lava dome. In addition, the formation of a poorly permeable carapace is likely to cause internal gas overpressure. Finally, a tectonic event associated to El Angel fault system or a volcano-tectonic earthquake due to the magma migration toward the surface might have contributed to the dome's destabilization.

The south-southeast direction of the explosion was clearly controlled by topographic elements that include the peak La Viuda and El Angel fault scarp (ENE in this sector). The decompression of the lava dome produced a lateral explosion that removed most of the dome and formed a high-energy turbulent stratified PDC. The front of the >170 m-thick PDC moved rapidly, allowing the PDC to cross several valleys and to overcome topographic obstacles such as Mindaburlo hill. Sedimentation was strongly controlled by the topography, and caused ponding of the most concentrated part of the PDC in valleys and segregation of more dilute PDCs able to spread further laterally and longitudinally. Taking into account the stratigraphy of the 3640–3510 BC PDC, the velocity estimated (120–135 m s^{-1} at 5 km from the source), and the historical

record of directed blasts (Belousov et al. 2007; Komorowski et al. 2013) it is probable that the PDC was initiated in only a few minutes. The directed blast was followed by a vertical eruption that produced a sub-Plinian column that lasted about 1 h (Table 7). When the eruptive column reached the low stratosphere it rapidly drifted to the west producing a pyroclastic fall in the Chachimbiro highlands.

Hazard assessment

The identification of the source and the dynamics of an eruption is critical for hazard assessment and monitoring purposes. Lava domes are common features in the Ecuadorian Volcanic Front, but the 3640–3510 BC eruption differs from other comparable eruptions in some aspects. There are only two documented rhyodacitic domes in the Ecuadorian Volcanic Front (EVF): (1) Pilongo, in the Iliniza volcanic complex (Hidalgo et al. 2007); and (2) Fuya-Fuya, in the Mojanda Fuya-Fuya volcanic complex (Robin et al. 2009). Pilongo is a moderate-size (650 m diameter, 240 m high) satellite dome, located 6 km northeast of Iliniza summit, and lies directly on top of a fault system traversing Iliniza volcano. Fuya-Fuya is a large (3 km diameter, 600–800 m high) polygenetic dome. None of these domes produced a directed blast. In the EVF, Guagua Pichincha, Imbabura, and Chachimbiro volcanoes have experienced directed blasts associated with giant landslides (Robin et al. 2008; Bernard et al. 2011; Le Pennec et al. 2011). Directed blasts, some related to giant landslides, have been documented at numerous volcanoes worldwide (Belousov et al. 2002; Boudon et al. 2005; Macías et al. 2010; Komorowski et al. 2013) and are thought to be a common phenomenon that must be taken into account when assessing volcanic hazards. The 3640–3510 BC eruption highlights the fact that satellite domes formed in a single eruption can also produce directed blasts. Such satellite domes also enlarge significantly the area potentially affected by high-energy PDCs. Accordingly, hazard maps must better take into account local tectonic elements. For monitoring purposes, the dome growth rate should be used to assess the probability of a dome blast, based on data from modern eruptions (Komorowski et al. 2013).

Conclusions

Our study provides evidence of a large eruption dated between 3640 and 3510 years BC. Mapping and sedimentological analysis indicate that the eruption was produced by the sudden decompression of a medium-sized rhyodacite satellite dome that extruded 6.3 km east of Chachimbiro central vent. Rock and mineral chemistry point out that the magma of this eruption came from a deep reservoir (~14.4 km deep) shared with the Chachimbiro feeding system. Then, it migrated along El Angel fault up to a shallower independent reservoir (~8.0 km deep) before reaching the surface.

While the surface of the dome was slowly cooling and outgassing, the internal pressure increased because gas and magma were fed into it, and pressure eventually surpassed the lava resistance and produced a violent directed blast. A tectonic or volcano-tectonic earthquake might also have triggered destabilization of the lava dome. The high velocity (>120 m s^{-1}) pyroclastic density current produced by dome decompression traveled more than 10 km and was able to cross several deep valleys and overpass a >200 m high hill 8 km from the source. It spread over 62 km^2 and destroyed a large area of the Urcuquí district, burying remains of human settlements. The directed blast was followed by a sub-Plinian eruption that produced a $7–11 \times 10^6$ m^3 (DRE) fallout deposit in Chachimbiro highlands.

This eruption was the largest from Chachimbiro volcanic complex in the last 6,000 years. Even though apparently rare, eruption of satellite domes must be considered for hazard assessment in the Ecuadorian Volcanic Front as they can produce highly explosive eruptions. In particular, the probability of a directed blast event must be considered as high in the case of a fast-growing dome.

Acknowledgments The sedimentological analysis (stratigraphy, grain-size distribution, and densitometry) of the PDC deposit has been funded with a Chancellor Grant of the Universidad San Francisco de Quito (P07AR71701USFQ2012-18). The ^{14}C datings, geochemical, and petrographic analysis, as well as the fieldwork for this study have been funded by the Institut de Recherche pour le Développement in association with the Instituto Geofísico de la Escuela Politécnica Nacional. This research has been completed in the context of a Laboratoire Mixte International "Séismes et Volcans dans les Andes du Nord". The authors thank Luc Ortlieb and the Laboratoire de Mesure du Carbone 14 for the ^{14}C datings. The authors also thank Celine Liorzou from the Université de Bretagne Occidentale for the whole-rock chemical analysis and Jean-Luc Devidal from the Laboratoire Magmas et Volcans of Blaise Pascal University (Clermont II) for his kind help with the microprobe analysis. The authors acknowledge the participation of Marion Bécouze, Celia Guergouz, and Francisco Herrera to perform the fieldwork. Thorough reviews by J.-C. Komorowski, J.D.L. White, and an anonymous reviewer greatly helped us to improve this manuscript.

References

Andersen DJ, Lindsley DH (1988) Internally consistent solution models for Fe-Mg-Mn oxides: Fe-Ti oxides. Am Mineral 73:714–726

Andersen DJ, Lindsley DH, Davidson PM (1998) QUILF: A program to assess equilibria among Fe-Mg-Ti oxides, pyroxenes, olivine, and quartz, New York

Andrade D, Martin H, Monzier M (2014) Restricciones y un posible modelo para la génesis de los magmas del volcán Pululahua (Ecuador). Revista EPN 33(2):112–121

Andrade D (2009) The influence of active tectonics on the structural development and flank collapse of ecuadorian arc volcanoes. PhD thesis, Université Blaise Pascal, Clermont-Ferrand-France

Andrews BJ, Manga M (2011) Effects of topography on pyroclastic density current runout and formation of coignimbrites. Geology 36(12):1099–1102. doi:10.1130/G32226.1

Auker MR, Sparks RSJ, Siebert L, Crosweller HS, Ewert J (2013) A statistical analysis of the global historical volcanic fatalities record. J Appl Volcanol 2:2. doi:10.1186/2191-5040-2-2

Bacon CR, Hirschmann MM (1988) Mg/Mn partitioning as a test equilibrium between coexisting Fe-Ti oxides. Am Mineral 73:57–61

Beate B (2001) Tefracronología Holocénica en el complejo Volcánico de Chachimbiro, prov. de Imbabura. Resumen en "Cuartas Jornadas en Ciencias de la Tierra", Escuela Politécnica Nacional, April 3–6, Quito (Ecuador), p 8

Belousov A (1996) Pyroclastic deposits of March 30, 1956 directed blast at Bezymianny volcano. Bull Volcanol 57:649–662

Belousov A, Voight B, Belousova M, Petukhin A (2002) Powerful pyroclastic surge in the May 8–10, 1997 explosive eruption of Bezymianny volcano, Kamchatka, Russia. Bull Volcanol 64:455–471

Belousov A, Voight B, Belousova M (2007) Directed blasts and blast-generated pyroclastic density currents: a comparison of the Bezymianny 1956, Mount St Helens 1980, and Soufrière Hills, Montserrat 1997 eruptions and deposits. Bull Volcanol 69:701–740

Bernard B, Robin C, Beate B, Hidalgo S (2011) Nuevo modelo evolutivo y actividad eruptiva reciente del volcán Chachimbiro. Extended abstract in the "7mas Jornadas en Ciencias de la Tierra", Escuela Politécnica Nacional, November 23–25, Quito (Ecuador), pp 119–122

Biass S, Bonadonna C (2011) A quantitative uncertainty assessment of eruptive parameters derived from tephra deposits: The example of two large eruptions of Cotopaxi volcano, Ecuador. Bull Volcanol 73: 73–90. doi:10.1007/s00445-010-0404-5

Bonadonna C, Costa A (2012) Estimating the volume of tephra deposits: A new simple strategy. Geology 40(5):415–418. doi:10.1130/G32769.1

Bonadonna C, Costa A (2013) Plume height, volume, and classification of explosive volcanic eruptions based on the Weibull function. Bull Volcanol 75:742. doi:10.1007/s00445-013-0742-1

Bonadonna C, Houghton BF (2005) Total grain-size distribution and volume of tephra fall deposits. Bull Volcanol 67:441–456. doi:10.1007/s00445-004-0386-2

Boudon G, Le Friant A, Villemant B, Viodé J-P (2005) Martinique. In: Lindsay JM, Robertson REA, Shepherd JB, Ali S (Eds.), Volcanic Hazard Atlas of the Lesser Antilles. Seismic Research Uni, The University of the West Indies, Trinidad and Tobago, WI, pp 126–145

Branney MJ, Kokelaar P (2002) Pyroclastic density currents and the sedimentation of ignimbrites. Geol Soc Lond, Mem 27:1–143

Bronk Ramsey C (2005) OxCal program v3.10 [software and online manual]. URL: http://www.rlaha.ox.ac.uk/oxcal/oxcal.htm. Accessed 13 January 2014

Burgisser A, Bergantz GW (2002) Reconciling pyroclastic flow and surge: the multiphase physics of pyroclastic density currents. Earth Planet Sci Lett 202:405–418

Calder ES, Cole PD, Dade WB, Druitt TH, Hoblitt RP, Huppert HE, Ritchie L, Sparks RSJ, Young SR (1999) Mobility of pyroclastic flows and surges at the Soufriere Hills Volcano, Montserrat. Geophys Res Lett 26:537–540

Cas RAF, Wright JV (1987) Volcanic successions. Modern and ancient. Allen and Unwin, London

Carey S, Sparks RSJ (1986) Quantitative models of the fallout and dispersal of tephra from volcanic eruption columns. Bull Volcanol 48:109–125

Charbonnier SJ, Germa A, Connor CB, Gertisser R, Preece K, Komorowski J-C, Lavigne F, Dixon T, Connor L (2013) Evaluation of the impact of the 2010 pyroclastic density currents at Merapi volcano from high-resolution satellite imagery, field investigations and numerical simulations. J Volcanol Geotherm Res 261:295–315. doi:10.1016/j.jvolgeores.2012.12.021

Cobeñas G, Thouret J-C, Bonadonna C, Boivin P (2012) The c.2030 yr BP Plinian eruption of El Misti volcano, Peru: eruption dynamics and hazard implications. J Volcanol Geotherm Res 241–242:105–120

Cotten J, Ledez A, Bau M, Caroff M, Maury RC, Dulski P, Fourcade S, Bohn M, Brousse R (1995) Origin of anomalous rare-earth element and yttrium enrichments in subaerially exposed basalts—evidence from French-Polynesia. Chem Geol 119:115–138

Crandell DR (1989) Gigantic debris avalanche of Pleistocene age from ancestral Mount Shasta volcano, California and debris-avalanche hazard zonation. USGS Bull, 1861

Crosweller HS, Arora B, Brown SK, Cottrell E, Deligne NI, Guerrero NO, Hobbs L, Kiyosugi K, Loughlin SC, Lowndes J, Nayembil M, Siebert L, Sparks RSJ, Takarada S, Venzke E (2012) Global database on large magnitude explosive volcanic eruptions (LaMEVE). J Appl Volcanol 1:4. doi:10.1186/2191-5040-1-4

Dade WB (2003) The emplacement of low-aspect ratio ignimbrites by turbulent parent flows. J Geophys Res 108(B4):2211. doi:10.1029/2001JB001010

Druitt TH (1998) Pyroclastic density currents. In: Gilbert JS and Sparks RSJ (eds) The physics of explosive volcanic eruptions. Geol Soc London Spec Publ, 145:145–182

Eychenne J, Le Pennec J-L, Ramón P, Yepes H (2013) Dynamics of explosive paroxysms at open-vent andesitic systems: high-resolution mass distribution analyses of the 2006 Tungurahua fall deposit (Ecuador). Earth Planet Sci Lett 361:343–355. doi:10.1016/j.epsl.2012.11.002

Fierstein J, Nathenson M (1992) Another look at the calculation of fallout tephra volumes. Bull Volcanol 54:156–167

Fisher RV (1990) Transport and deposition of a pyroclastic surge across an area of high relief: the 18 May 1980 eruption of Mount St. Helens, Washington. Geol Soc Am Bull 102:1038–1054

Fisher RV, Schmincke H-U (1984) Pyroclastic rocks. Springer, Berlin

Francis PW, Baker MCW (1977) Mobility of pyroclastic flows. Nature 270:164–165

Freundt A, Wilson CJN, Carey SN (2000) Ignimbrites and block-and-ash deposits. In: Sigurdsson H, Houghton B, McNutt SR, Rymer H, Stix J (eds) Encyclopedia of volcanoes. Academic, London, pp 581–599

Gardner JE, Tait S (2000) The caldera-forming eruption of Volcán Ceboruco, Mexico. Bull Volcanol 62(1):20–33. doi:10.1007/s004450050288

Ghiorso MS, Evans BW (2008) Thermodynamics of rhombohedral oxide solid solutions and a revision of the Fe-Ti two-oxide geothermometer and oxygen-barometer. Am J Sci 308:957–1039

Glicken H (1996) Rockslide-debris avalanche of May 18, 1980, Mount St. Helens volcano, Washington. Cascades Volcano Observatory, Vancouver, Open-file Report, 96–677

Hall ML, Mothes PA (1997) El Origen y Edad de la Cangahua Superior, Valle de Tumbaco, Ecuador. In: Zebrowski C, Quantin P, Trujillo G, Memoirs—Suelos Volcánicos Endurecidos. III Simposio Internacional (ORSTOM–Quito. Dic. 1996), pp. 19–28

Hall ML, Mothes PA (2008) Quilotoa volcano—Ecuador: an overview of young dacitic volcanism in a lake-filled caldera. J Volcanol Geotherm Res 176:44–55. doi:10.1016/j.jvolgeores.2008.01.025

Hayashi JN, Self S (1992) A comparison of pyroclastic flow and debris avalanche mobility. J Geophys Res 97:9063–9071

Heim A (1932) Bergsturz und Menschenleben. Fretz und Wasmuth, Zürich

Hoblitt RP, Miller CD, Vallance JW (1981) Origin and stratigraphy of the deposit produced by the May 18 directed blast. In: Lipman PW, Mullineaux DR (eds) The 1980 eruptions of Mount St. Helens, Washington. USGS Prof Paper, 1250:401–419

Houghton BF, Wilson CJN (1989) A vesicularity index for pyroclastic rocks. Bull Volcanol 51:451–462

Hidalgo S, Monzier M, Martin H, Chazot G, Eissen J-P, Cotten J (2007) Adakitic magmas in the Ecuadorian Volcanic Front: petrogenesis of the Iliniza volcanic complex (Ecuador). J Volcanol Geotherm Res 159:366–392

Hidalgo S, Monzier M, Almeida E, Chazot G, Eissen J-P, van der Plicht J, Hall ML (2008) Late Pleistocene and Holocene activity of the Atacazo–Ninahuilca volcanic complex (Ecuador). J Volcanol Geotherm Res 176:16–26. doi:10.1016/j.jvolgeores.2008.05.017

Inman DL (1952) Measures for describing the size distribution of sediments. J Sed Petrol 22:125–145

Johnson MC, Rutherford MJ (1989) Experimental calibration of the aluminium-in-hornblende geobarometer with application to Long Valley caldera (California) volcanic rocks. Geology 17: 837–841

Komorowski J-C, Jenkins S, Baxter PJ, Picquout A, Lavigne F, Charbonnier S, Gertisser R, Preece K, Cholik N, Budi-Santoso A, Surono (2013) Paroxysmal dome explosion during the Merapi 2010 eruption: processes and facies relationships of associated high-energy pyroclastic density currents. J Volcanol Geotherm Res 261: 260–294. doi:10.1016/j.jvolgeores.2013.01.007

Leake BE, Woolley AR, Arps CES, Birch WD, Gilbert MC, Grice JD, Hawthorne FC, Kato A, Kisch HJ, Krivovichev VG, Linthout K, Laird J, Mandarino JA, Maresch WV, Nickel EH, Rock NMS, Schumacher JC, Smith DC, Stephenson NCN, Ungaretti L, Whittaker EJW, Guo YZ (1997) Nomenclature of amphiboles: report of the subcommittee on amphiboles of the International Mineralogical Association, Commission on New Minerals and Mineral Names. Mineral Mag 61:295–321

Legros F (2000) Minimum volume of a tephra fallout deposit estimated from a single isopach. J Volcanol Geotherm Res 96:25–32

Le Pennec J-L, Ruiz AG, Eissen J-P, Hall ML, Fornari M (2011) Identifying potentially active volcanoes in the Andes: radiometric evidence for late Pleistocene-early Holocene eruptions at Volcán Imbabura, Ecuador. J Volcanol Geotherm Res 206:121–135

Macías JL, Arce JL, García-Palomo A, Mora JC, Layer PW, Espíndola JM (2010) Late-Pleistocene flank collapse triggered by dome growth at Tacaná volcano, México-Guatemala, and its relationship to the regional stress regime. Bull Volcanol 72:33–53. doi:10.1007/s00445-009-0303-9

Mastin LG, Guffanti M, Servranckx R, Webley P, Barsotti S, Dean K, Durant A, Ewert JW, Neri A, Rose WI, Schneider D, Siebert L, Stunder B, Swanson G, Tupper A, Volentik A, Waythomas CF (2009) A multidisciplinary effort to assign realistic source parameters to models of volcanic ash-cloud transport and dispersion during eruptions. J Volcanol Geotherm Res 186(1–2):10–21

McGimsey RG, Neal CA, Riley CM (2001) Areal distribution, thickness, mass, volume, and grain-size of tephra-fall deposits from the 1992 eruptions of Crater Peak vent, Mt. Spurr volcano, Alaska. USGS Report 01–370

Monzier M, Robin C, Hall ML, Cotten J, Mothes P, Eissen J-P, Samaniego P (1997) Les adakites d'Équateur : modèle préliminaire. Comptes Rendus Acad Sci, Paris, 324 (IIa): pp 545–552

Mook WG, Streurman HJ (1983) Physical and chemical aspects of radiocarbon dating. PACT Publications 8:31–55

Moreira Pino M (2012) Prospección arqueológica en el sector de la implementación del proyecto Yachay (660 hectáreas)—cuidad del conocimiento Ecuador, provincia de Imbabura, cantón Urcuquí. INPC Report

Newhall CG, Self S (1982) The volcanic explosivity index (VEI): an estimate of explosive magnitude for historical volcanism. J Geophys Res 87:1231–1238

Oxford-Economics (2010) The economic impacts of air travel restrictions due to volcanic ash report for airbus. Oxford Economics Report, Oxford, UK, p. 12

Peccerillo A, Taylor SR (1976) Geochemistry of Eocene calc-alkaline volcanic rocks from the Kastamonu area, Northern Turkey. Contrib Mineral Petrol 58:63–81

Pitari G, Mancini E (2002) Short-term climatic impact of the 1991 volcanic eruption of Mt. Pinatubo and effects on atmospheric tracers. Nat Hazards Earth Syst Sci 2:91–108

Putirka KD (2008) Thermometers and barometers for volcanic systems. Rev Mineral and Geochem 69:61–120

Pyle DM (1989) The thickness, volume and grainsize of tephra fall deposits. Bull Volcanol 51:1–15

Pyle DM (2000) Sizes of volcanic eruptions. In: Sigurdsson H, Houghton B, McNutt SR, Rymer H, Stix J (eds) Encyclopedia of volcanoes. Academic, London, pp 263–269

Reimer PJ, Baillie MGL, Bard E, Bayliss A, Beck JW, Bertrand CJH, Blackwell PG, Buck CE, Burr GS, Cutler KB, Damon PE, Edwards RL, Fairbanks RG, Friedrich M, Guilderson TP, Hogg AG, Hughen KA, Kromer B, McCormac G, Manning S, Bronk Ramsey C, Reimer RW, Remmele S, Southon JR, Stuiver M, Talamo S, Taylor FW, van der Plicht J, Weyhenmeyer CE (2004) IntCal04, terrestrial radiocarbon age calibration, 0–26 cal kyr BP. Radiocarbon 46(3):1029–1058

Ridolfi F, Renzulli A, Puerini M (2010) Stability and chemical equilibrium of amphibole in calc-alkaline magmas: an overview, new thermobarometric formulations and application to subduction-related volcanoes. Contrib Mineral Petrol 160(1):45–66. doi:10.1007/s00410-009-0465-7

Robin C, Samaniego P, Le Pennec J-L, Mothes P, van der Plicht J (2008) Late Holocene phases of dome growth and Plinian activity at Guagua Pichincha volcano (Ecuador). J Volcanol Geotherm Res 176:7–15. doi:10.1016/j.jvolgeores.2007.10.008

Robin C, Eissen J-P, Samaniego P, Martin H, Hall ML, Cotten J (2009) Evolution of the late Pleistocene Mojanda-Fuya Fuya volcanic complex (Ecuador), by progressive adakitic involvement in mantle magma sources. Bull Volcanol 71:233–258. doi:10.1007/s00445-008-0219-9

Rutherford MJ, Hill PM (1993) Magma ascent rates from amphibole breakdown: an experimental study applied to the 1980–1986 Mount St. Helens eruptions J Geophys Res 98(B11): 19667–19685

Saucedo R, Macías JL, Sheridan MF, Bursik MI, Komorowski J-C (2005) Modeling of pyroclastic flows of Colima Volcano, Mexico: implications for hazard assessment. J Volcanol Geotherm Res 139:103–115. doi:10.1016/j.jvolgeores.2004.06.019

Sun SS, McDonough WF (1989) Chemical and isotopic systematics of ocean basalts: Implication for mantle composition and processes. In: Saunders AD and Norry MJ, Eds., Magmatism in Ocean Basins. Geol Soc London Spec Publ, 42:313–345

Valentine GA (1987) Stratified flow in pyroclastic surges. Bull Volcanol 49:616–630

Valentine GA, Fisher RV (2000) Pyroclastic surges and blasts. In: Sigurdsson H, Houghton B, McNutt SR, Rymer H, Stix J (eds) Encyclopedia of volcanoes. Academic, London, pp 571–580

Vallejo C, Spikings RA, Winkler W, Luzieux L, Chew D, Page L (2006) The early interaction between the Caribbean Plateau and the NW South American plate. Terra Nova 18:264–269

Voight B, Komorowski J-C, Norton GE, Belousov AB, Belousova M, Boudon G, Francis PW, Franz W, Heinrich P, Sparks RSJ, Young SR (2002) The 1997 Boxing Day Sector Collapse and Debris Avalanche, Soufriere Hills Volcano, Montserrat, W.I. In: TH Druitt, BP Kokelaar (Eds), The eruption of Soufrière Hills Volcano, Montserrat, from 1995 to 1999. Geol Soc London, Memoirs, 21, 363–407

Von Hillebrandt C (1989) Estudio geovolcanológico del Complejo Volcánico Cuicocha-Cotacachi y sus aplicaciones. Provincia de Imbabura, Tesis de Ingeniería, Escuela Politécnica Nacional, Quito-Ecuador

Walker G (1971) Grain-size characteristics of pyroclastic deposits. J Geol 79:696–714

White JDL, Houghton BF (2006) Primary volcanoclastic rocks. Geology 34(8):677–680. doi:10.1130/G22346.1

Wilson CJN, Houghton BF (2000) Pyroclastic transport and deposition. In: Sigurdsson H, Houghton B, McNutt SR, Rymer H, Stix J (eds) Encyclopedia of volcanoes. Academic, London, pp 545–554

Zeidler JA (2008) The Ecuadorian formative. In: Silverman H, Isbell WH (eds) The handbook of South American archaeology. Springer, New York, pp 459–488